



HAL
open science

The Syabru-Bensi hydrothermal system in central Nepal:

1. Characterization of carbon dioxide and radon fluxes

Frédéric Girault, Frédéric Perrier, Robin Crockett, Mukunda Bhattarai, Bharat Prasad Koirala, Christian France-Lanord, Pierre Agrinier, Magali Ader, Frédéric Fluteau, Claire Gréau, et al.

► To cite this version:

Frédéric Girault, Frédéric Perrier, Robin Crockett, Mukunda Bhattarai, Bharat Prasad Koirala, et al.. The Syabru-Bensi hydrothermal system in central Nepal: 1. Characterization of carbon dioxide and radon fluxes. *Journal of Geophysical Research: Solid Earth*, 2014, 10.1002/2013JB010301 . insu-01295841

HAL Id: insu-01295841

<https://insu.hal.science/insu-01295841>

Submitted on 31 Mar 2016

HAL is a multi-disciplinary open access archive for the deposit and dissemination of scientific research documents, whether they are published or not. The documents may come from teaching and research institutions in France or abroad, or from public or private research centers.

L'archive ouverte pluridisciplinaire **HAL**, est destinée au dépôt et à la diffusion de documents scientifiques de niveau recherche, publiés ou non, émanant des établissements d'enseignement et de recherche français ou étrangers, des laboratoires publics ou privés.

RESEARCH ARTICLE

10.1002/2013JB010301

This is a companion paper to *Girault and Perrier* [2014], doi:10.1002/2013JB010302.

Key Points:

- The Syabru-Bensi hydrothermal system (SBHS) shows large CO₂ and radon fluxes
- Radon gas is a proxy of its carrier gas CO₂ and may facilitate monitoring
- The SBHS emerges as a unique medium-scale system in a seismically active region

Supporting Information:

- Readme
- Table S1
- Texts S1–S3

Correspondence to:

F. Girault,
girault@ipgp.fr

Citation:

Girault, F., et al. (2014), The Syabru-Bensi hydrothermal system in central Nepal: 1. Characterization of carbon dioxide and radon fluxes, *J. Geophys. Res. Solid Earth*, 119, 4017–4055, doi:10.1002/2013JB010301.

Received 18 APR 2013

Accepted 1 APR 2014

Accepted article online 3 APR 2014

Published online 12 MAY 2014

The Syabru-Bensi hydrothermal system in central Nepal: 1. Characterization of carbon dioxide and radon fluxes

Frédéric Girault¹, Frédéric Perrier¹, Robin Crockett², Mukunda Bhattarai³, Bharat Prasad Koirala³, Christian France-Lanord⁴, Pierre Agrinier⁵, Magali Ader⁵, Frédéric Fluteau⁶, Claire Gréau⁷, and Manuel Moreira⁷

¹Équipe de Géomagnétisme, Institut de Physique du Globe de Paris, Sorbonne Paris Cité, Université Paris Diderot, CNRS UMR7154, Paris, France, ²Department of Environmental and Geographical Sciences, School of Science and Technology, University of Northampton, Northampton, UK, ³National Seismological Centre, Department of Mines and Geology, Kathmandu, Nepal, ⁴Centre de Recherches Pétrographiques et Géochimiques, CNRS, Université de Nancy, Vandœuvre-lès-Nancy, France, ⁵Équipe de Physico-chimie des Fluides Géologiques, Institut de Physique du Globe de Paris, Sorbonne Paris Cité, Université Paris Diderot, CNRS UMR7154, Paris, France, ⁶Équipe de Paléomagnétisme, Institut de Physique du Globe de Paris, Sorbonne Paris Cité, Université Paris Diderot, CNRS UMR7154, Paris, France, ⁷Équipe de Géochimie et Cosmochimie, Institut de Physique du Globe de Paris, Sorbonne Paris Cité, Université Paris Diderot, Paris, France

Abstract The Syabru-Bensi hydrothermal system (SBHS), located at the Main Central Thrust zone in central Nepal, is characterized by hot (30–62°C) water springs and cold (<35°C) carbon dioxide (CO₂) degassing areas. From 2007 to 2011, five gas zones (GZ1–GZ5) were studied, with more than 1600 CO₂ and 850 radon flux measurements, with complementary self-potential data, thermal infrared imaging, and effective radium concentration of soils. Measurement uncertainties were evaluated in the field. CO₂ and radon fluxes vary over 5 to 6 orders of magnitude, reaching exceptional maximum values of $236 \pm 50 \text{ kg m}^{-2} \text{ d}^{-1}$ and $38.5 \pm 8.0 \text{ Bq m}^{-2} \text{ s}^{-1}$, with estimated integrated discharges over all gas zones of $5.9 \pm 1.6 \text{ t d}^{-1}$ and $140 \pm 30 \text{ MBq d}^{-1}$, respectively. Soil-gas radon concentration is $40 \times 10^3 \text{ Bq m}^{-3}$ in GZ1–GZ2 and $70 \times 10^3 \text{ Bq m}^{-3}$ in GZ3–GZ4. Strong relationships between CO₂ and radon fluxes in all gas zones (correlation coefficient $R = 0.86 \pm 0.02$) indicate related gas transport mechanisms and demonstrate that radon can be considered as a relevant proxy for CO₂. CO₂ carbon isotopic ratios ($\delta^{13}\text{C}$ from -1.7 ± 0.1 to $-0.5 \pm 0.1\%$), with the absence of mantle signature (helium isotopic ratios $R/R_A < 0.05$), suggest metamorphic decarbonation at depth. Thus, the SBHS emerges as a unique geosystem with significant deep origin CO₂ discharge located in a seismically active region, where we can test methodological issues and our understanding of transport properties and fluid circulations in the subsurface.

1. Introduction

The global mapping of carbon dioxide (CO₂) emissions is one of the most active research subjects throughout the world [e.g., *Bréon and Ciais*, 2010]. Among other pending questions regarding the sources and sinks, the CO₂ budget of active orogens remains poorly understood [*Gaillardet and Galy*, 2008], and this is particularly the case in the Himalayas, the Earth's largest current orogen. More generally, studies that have dealt with the spatial distribution of CO₂ fluxes at the Earth's surface were carried out primarily near volcanoes [e.g., *Baubron et al.*, 1990; *Farrar et al.*, 1995; *Giammanco et al.*, 1995; *Chiodini et al.*, 1998; *Hernández et al.*, 1998]. Recently, many studies have focused on various natural systems, e.g., volcanic [e.g., *Chiodini et al.*, 2005; *Toutain et al.*, 2009; *Viveiros et al.*, 2009; *Finizola et al.*, 2010; *Granieri et al.*, 2010; *Di Napoli et al.*, 2011; *Federico et al.*, 2011; *Mazot et al.*, 2011, 2013; *Carapezza et al.*, 2012; *Inguaggiato et al.*, 2012; *Hernández et al.*, 2012a, 2012b; *Rinaldi et al.*, 2012; *Tassi et al.*, 2013], geothermal [e.g., *D'Alessandro et al.*, 2006; *Fridriksson et al.*, 2006; *Werner and Cardellini*, 2006; *Annunziatellis et al.*, 2008; *Rodrigo-Naharro et al.*, 2013], and hydrothermal geosystems [e.g., *Gerlach et al.*, 2001; *Lewicki et al.*, 2008, 2012, 2013; *Werner et al.*, 2008; *Rissmann et al.*, 2012]. However, only a few studies were performed in low temperature (<50°C) CO₂ degassing areas [e.g., *Mörner and Etiope*, 2002], such as mofette sites [e.g., *Italiano et al.*, 2000; *Rogie et al.*, 2000; *Vodnik et al.*, 2009; *Chiodini et al.*, 2010; *Kämpf et al.*, 2013; *Bräuer et al.*, 2013], as well as in fault-related areas [e.g., *Etiope*, 1999; *Lewicki and Brantley*, 2000; *Lewicki et al.*, 2003a; *Ciotoli et al.*, 2007] and, more rarely, in the largest orogens [*Perrier et al.*, 2009; *Richon et al.*, 2010]. In addition to the

contribution to global CO₂ budget, CO₂ degassing of large orogens might appear as a crustal parameter sensitive to long-term and short-term effects, such as strain buildup during interseismic periods and stress release during earthquakes, respectively.

The Himalayan range, with typical current collision/shortening rates of 18–21 mm yr⁻¹ in Nepal [e.g., *Bettinelli et al.*, 2006; *Ader et al.*, 2012], is a potential location for megaquakes [*Avouac et al.*, 2001; *Bollinger et al.*, 2004; *Sapkota et al.*, 2013], and therefore, monitoring of such gaseous emissions might allow observation of potential earthquake precursors. Radon-222 is a radioactive gas with a half-life of 3.8232 ± 0.0004 d [*Collé*, 1995] and is the alpha decay product of radium-226, with a half-life of 1600 ± 7 yr [*Duchemin et al.*, 1994], in the uranium-238 decay chain. Precursory emissions of radon [*Toutain and Baubron*, 1999; *Crockett et al.*, 2006; *King et al.*, 2006; *Ghosh et al.*, 2009; *Crockett and Gillmore*, 2010] have also been reported previously in the Himalayas [*Virk and Singh*, 1994; *Walia et al.*, 2006]. Nevertheless, such observations, which are only partially analyzed and understood, are the subject of much skepticism [e.g., *Geller*, 2011]. The current understanding of gas sources, as well as midcrust permeability and deformation, is still largely insufficient to propose a meaningful model of gas emissions in association with the earthquake cycle [e.g., *Manning and Ingebritsen*, 1999; *Rojstaczer et al.*, 2008; *Manga et al.*, 2012].

Cold (<35°C) degassing of CO₂ containing radon has been identified since 2005 in the Syabru-Bensi hydrothermal system (SBHS), located in the upper Trisuli Valley, central Nepal [*Perrier et al.*, 2009]. CO₂ fluxes measured on the ground reached maxima of $19,000 \text{ g m}^{-2} \text{ d}^{-1}$ [*Perrier et al.*, 2009], a value typically associated with volcanoes [e.g., *Granieri et al.*, 2010; *Carapezza et al.*, 2011], while the total CO₂ discharge rate near the main hot springs was estimated to be only $1.0 \pm 0.3 \text{ t d}^{-1}$ [*Perrier et al.*, 2009]. Radon fluxes measured on the ground reached maxima of $2.0 \text{ Bq m}^{-2} \text{ s}^{-1}$ [*Perrier et al.*, 2009], an uncommonly large value more typically associated with former uranium mining/milling sites [e.g., *Mudd*, 2008; *Lavrova and Voitsekhovych*, 2013]. While radon might be a unique asset for temporal monitoring, previous studies have been unsuccessful in establishing a consistent relationship between radon and CO₂. Furthermore, only a small area of the hydrothermal system could then be explored, and so generally applicable modeling of gas transport could not be attempted.

In this paper, we report comprehensive results obtained in five degassing areas (“gas zone,” GZ1–GZ5) in the SBHS studied between September 2007 and January 2011. In the following sections, we describe these zones and the prevailing meteorological conditions. We also outline the methods, with fuller descriptions presented in the supporting information, and then present and discuss the results as compared with other sites worldwide. A detailed discussion of the significance and modeling of the radon signature is presented in the companion paper [*Girault and Perrier*, 2014].

2. Description of the SBHS

The SBHS is located at 1400 m above sea level in central Nepal, 60 km north of Kathmandu and 15 km south of the Tibetan border (Figure 1). This site is oriented NE-SW and is bounded at its northeastern part by the confluence of the Bhote Kosi River flowing from the north and the Langtang River flowing from the southeast, creating the Trisuli River (also named Bhote Kosi at this location) flowing to the southwest, and at its southwestern part by the bridge over the Trisuli River. It occupies a surface area of circa 0.86 km^2 . Various passable roads intersect at the Syabru-Bensi village, with the most recent, completed in 2010, heading north to Tibet along the Bhote Kosi River.

2.1. Geological and Hydrothermal Contexts

The geology of the site is dominated by the presence of the Main Central Thrust (MCT) zone. This shear zone, which is insufficiently well established [e.g., *Searle et al.*, 2008], is oriented circa 40°N and is generated by one of the main thrusts of the Himalayan Range, related at depth to the décollement of the Main Himalayan Thrust (MHT) [*Upreti*, 1999; *Guillot*, 1999]. The MCT places high-grade metamorphic crystalline units of the Greater Himalayan Sequence (GHS) southward over low-grade metamorphic sedimentary units of the Lesser Himalayan Sequence (LHS). This tectonic process is one of the causes invoked to explain the observed inverted metamorphism in the Himalayas [*Beysac et al.*, 2004; *Guillot et al.*, 2008]. In addition, intense seismicity is observed [*Pandey et al.*, 1995, 1999] between circa 10 and 25 km depth below the MCT, close to a location where a high-conductivity zone was identified [*Lemonnier et al.*, 1999], which suggests that this might also be the nucleation zone of large earthquakes [*Avouac*, 2003].

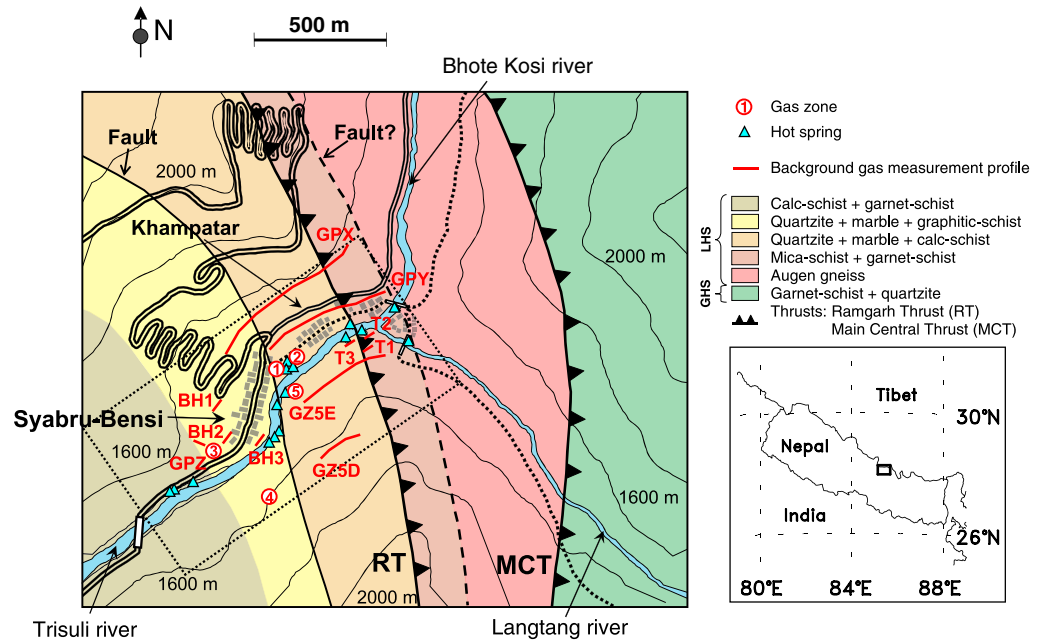


Figure 1. Geological map of the Syabru-Bensi hydrothermal system in central Nepal, with hot springs, gas zones, and background gas profiles. Dotted box defines the SBHS area (circa 0.86 km²). The inset shows the site location within Nepal. The geological map is a compilation from different contributions [Macfarlane et al., 1992; Parrish and Hodges, 1996; Takagi et al., 2003; Kohn, 2008], but also from our own fieldwork and observations [Girault et al., 2012], in particular concerning the position of the thrusts and the augen gneisses. The labels GPX, GPY, GPZ, BH1, BH2, and BH3 on the west bank of the Trisuli River and T1, T2, T3, GZ5D, and GZ5E on the east bank refer to the background gas profiles.

The MCT zone is also characterized by several other faults, such as the Ramgarh Thrust (RT) (Figure 1). This important thrust places older Paleoproterozoic LHS rocks upon younger Precambrian LHS units; it can be related at depth to the MCT or the MHT independently [Pearson and DeCelles, 2005]. In the upper Trisuli Valley, typically, the oldest rocks (circa 1.88 Ga) are the augen gneisses (Figure 1) [Kohn et al., 2010]. These rocks have similar characteristics to the Ulleri augen gneisses which are dated at circa 1.7–1.9 Ga [Upreti, 1999; Goscombe et al., 2006; Kohn et al., 2010]. Moreover, other more localized, secondary faults or shear zones can be mapped in the field, associated with the occurrence of black schist and the separation of graphitic schist and calc schist formations (Figure 1). The observed LHS rocks can be grouped into three groups, according to the presence of calc schist, garnet schist, graphitic schist, and also of quartzite and marble layers. Between the RT and the MCT, mica schist, garnet schist, and augen gneiss are observed [Girault et al., 2012]. The garnet schist unit is the first occurrence of the GHS (in green in Figure 1), while the augen gneiss formation is here incorporated in the LHS [Upreti, 1999].

The MCT shear zone is characterized by hydrothermal circulations and a large geothermal gradient of circa $75 \pm 8^\circ\text{C km}^{-1}$ [Derry et al., 2009]. The SBHS includes several hot springs, mainly located along the Trisuli River (Figures 1, 2a, and 2b). The main hot springs were studied first by Kotarba [1986] and are characterized by flow rates from 0.082 ± 0.006 to $0.36 \pm 0.03 \text{ L s}^{-1}$, temperatures from 30 to 62°C, alkalinity load reaching 25 mmol L^{-1} , and total absence of bubbling [Evans et al., 2004, 2008; Becker, 2005; Perrier et al., 2009]. Numerous secondary hot and cold water seepages, easier to observe during the dry winter season, occur along the river, sometimes associated with iron oxide deposits. Also, it is thought that there are additional unidentified hot springs that discharge directly from the river bed into the river.

2.2. The Gas Zones and Background Areas

Five gas zones were studied in the SBHS (total area circa 21,550 m²), three being located on the west bank of the Trisuli River (GZ1–GZ3) and two on the east bank (GZ4 and GZ5). These are all characterized by natural degassing from the ground, sometimes including mofette-like degassing.

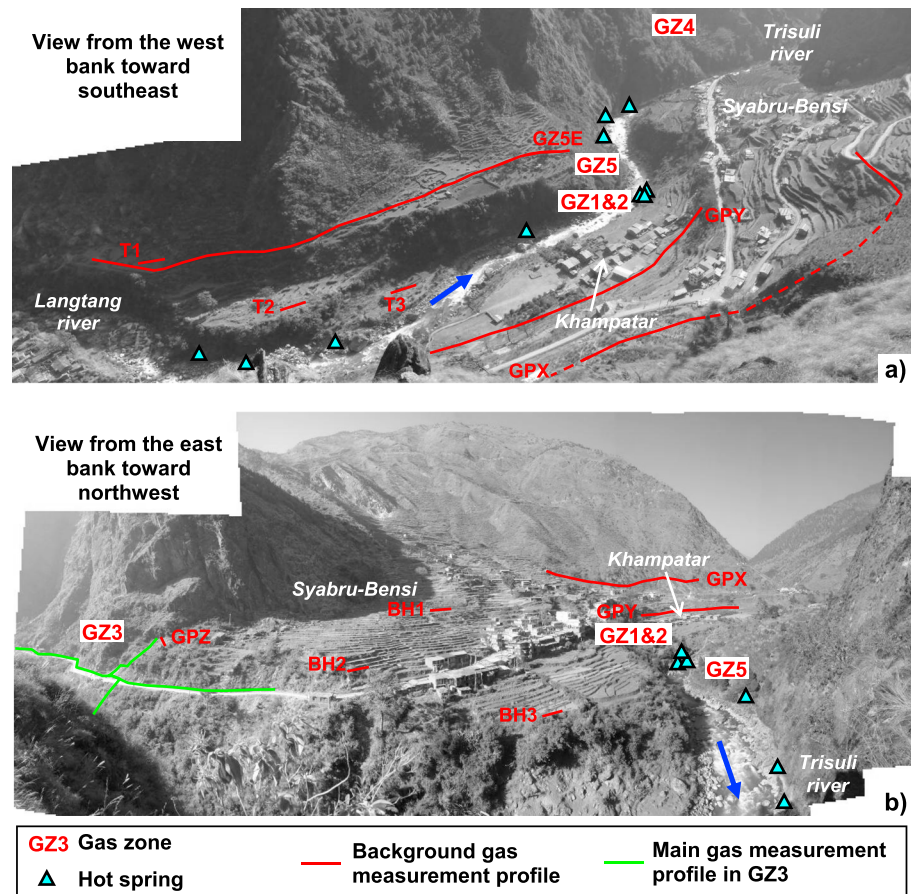


Figure 2. View toward (a) southeast and (b) northwest of the Syabru-Bensi hydrothermal system in central Nepal, with the position of hot springs, gas zones, and background gas profiles. Photographs were taken in 2008. The labels GPX, GPY, GPZ, BH1, BH2, and BH3 on the west bank of the Trisuli River and T1, T2, T3, and GZ5E on the east bank refer to the background gas profiles.

GZ1 (circa 500 m²) was the first gas zone discovered in the SBHS [Perrier *et al.*, 2009], which was also found to be characterized by a dipolar self-potential (SP) anomaly [Byrdina *et al.*, 2009]. This site is located at an altitude of 1425 m on a partly collapsed river terrace, just below the Syabru-Bensi village, near the main hot springs (Figures 1, 2a, and 2b). The central area is clear of vegetation, but the outer margins have been cultivated. GZ1, pervaded by a strong smell of H₂S, included three distinct subzones, with cavities in the terrace on the northern side. In the cavities, the soil is dark, rich in organic matter and in sulphate and sulphur deposits. In cavities 1A (left) and 1B (middle), it is possible to hear the whistling of the gas, with bubbling when water is present, whereas these phenomena are not observable in cavity 2 (right).

GZ2 (circa 150 m²) is located at an altitude of 1420 m (Figures 1, 2a, and 2b) in the vicinity of GZ1 just above the cemented basins of the main hot springs. The area is mainly characterized by an extensive recess where sulphur deposits occur and H₂S is detected. This site is a small collapsing terrace where several boulders of calc schist and mica schist are present, coming from the debris slope deposits located just above the terrace. The soil is dark and rich in organic matter at the southern part of the terrace and sandier at its northern part.

GZ3 (circa 5400 m²) is located at an altitude of 1410 m in the graphitic schist layer, circa 100 m south from the gate of the Syabru-Bensi village [Girault *et al.*, 2009] and circa 500 m away from any significant hot springs of the SBHS (Figures 1 and 2b). The site is characterized by several boulders of calc schist and garnet schist. The soil is muscovite-rich and sandy. Warm minor seepage points were discovered below GZ3 along the Trisuli River, southward from the main site (Figure 1). This site was substantially altered by the construction of the new road in late 2010.

GZ4 (circa 2000 m²) is the most elevated of the five gas zones, located at an altitude of 1465 m (Figures 1 and 2a, top right) opposite GZ3 on the left bank of the river. GZ4 is located in the same graphitic schist layer as GZ3, bordered above by a scarp of white marble containing a cavity from which H₂S emerges and where dead birds and young animals were discovered on the ground. In the cavity, covered by sulphates and travertine deposits, the soil is extremely dark and rich in organic matter, whereas it is less rich in organic matter and sandier along the gas profiles carried out below the cavity. Below GZ4, several hot springs are present (Figures 1 and 2a) near the Trisuli River.

GZ5 (circa 13,500 m²) is located at an altitude of circa 1440 m opposite the main hot springs, GZ1 and GZ2 (Figures 1, 2a, and 2b). This site is located on a cultivated river bed terrace characterized by debris slope deposits mainly composed of rocks belonging to calc schist, mica schist, and garnet schist layers. The soil is light brown, sometimes sandy and quite rich in organic matter.

In addition to the five gas zones, we selected zones, referred to as background sites, where we did not expect gas emission and where we could characterize the local conditions in the absence of gas. We defined 11 background sites (Figures 1, 2a, and 2b), chosen to encircle as much as possible the known gas zones. These background sites are labeled as follows: profiles GPX, GPY, GPZ (Figures 2a and 2b), BH1, BH2, and BH3 (Figure 2b) on the west bank of the Trisuli River, and profiles T1, T2, T3, GZ5E (Figure 2a), and GZ5D (Figures 1 and 12) on the east bank.

Three background sites are located in the same geological formation but in various fields [Girault, 2011]: an uncultivated field with gray soil rich in graphitic schist alteration products (BH1), a cultivated rice field with dark soil rich in graphitic schist alteration products (BH2), and a cultivated lentil field with gray sandy soil (BH3). Three other background sites are located on different river terraces on the east bank [Girault *et al.*, 2011b]: a wheat field with black soil rich in organic matter (T1), grazing land with gray muscovite-rich soil (T2), and dry land with sandy soil (T3). The background site GZ5D is located on a debris cone and calc schist bedrock, whereas GZ5E is on the same river terrace as T1. Finally, on the west bank, three sites are characterized by alternating debris cones, bedrock and uncultivated terraces (GPX), crop field terraces above GZ1 (GPY), and uncultivated river terraces above GZ3 (GPZ).

2.3. Meteorological Context

The SBHS is located in the northern Himalayas and benefits from a rain shadow effect of the Gosainkunda range. The dry season and the monsoon period occur from December to February and from June to September, respectively. The mean annual precipitation in Syabru-Bensi can be estimated as 1830, 1110, and 1330 mm in 2008, 2009, and 2010, respectively, using the rainfall data recorded at Timure, 10.5 km north, and Dhunche, 7 km south (Nepal Department of Meteorology, Kathmandu). The mean annual air temperature is 19°C, with annual minimum and maximum temperatures of 0°C (late January) and 28°C (early June, during the monsoon). The diurnal air temperature variation is fairly constant throughout the year at ±20°C about the diurnal mean.

It was observed that the CO₂ and radon fluxes were approximately constant (to first order) irrespective of the season and thus largely independent of any rainfall effect [Girault *et al.*, 2009]. This observation is supported by continuous radon monitoring over a 2 year period (2008 and 2009) that shows that the monsoon had negligible effect on the advective gas zones [Richon *et al.*, 2011]. This temporal stability of the gas zones and their invariance with the meteorological perturbations are particularly interesting for potential future long-term monitoring to search for possible relationships between geophysical stress changes at depth and gas emissions at the surface. The seasonal stability of GZ1 is further investigated below.

3. Measurement Methods

In this section, the general principles of the techniques and the main sources of uncertainties are outlined. The details of the techniques are expanded in Text S1 in the supporting information.

3.1. Measurement of CO₂ Flux

The accumulation chamber is the preferred technique for anomalous degassing areas such as those found in volcanic and hydrothermal contexts and therefore was used to measure the CO₂ flux (Φ_{CO_2}) [Chiodini *et al.*, 1998;

Welles *et al.*, 2001]. The CO₂ flux, usually expressed in g m⁻² d⁻¹, is directly related to the slope at the origin of the CO₂ accumulation curve ($dC/dt|_{t=0}$) according to [Chiodini *et al.*, 1998]:

$$\Phi_{\text{CO}_2} = \frac{P_{\text{atm}} M_{\text{CO}_2}}{RT} \left. \frac{V dC}{S dt} \right|_{t=0}, \quad (1)$$

where C is the CO₂ concentration, P_{atm} is the mean atmospheric pressure, M_{CO_2} is the molar mass of CO₂, R is the ideal gas constant, T is the ambient temperature, and V and S are chamber volume and footprint area, respectively.

Before measurement, vegetation was removed, and 3–5 cm of soil was brushed to prepare a relatively flat and homogeneous emplacement for the chamber. Wet soil was plastered around the base of the chamber to provide a seal. From summer 2007 to January 2011, various types of chambers with different sizes and shapes were used. The most commonly used chambers had a volume of 0.0085 m³ and a footprint area of 0.092 m².

The following sensors were used to measure CO₂ concentration in the chamber, all based on infrared absorption of gaseous CO₂: Testo™ sensors (Testo™ 535, Testo AG, Germany), Airwatch™ sensors (Airwatch™ PM 1500, Geotechnical Instruments Ltd., UK), and, since 2010, the semiautomatic Vaisala™ sensor (Vaisala™ CARBOCAP® Hand-Held GM70, Finland), which was used for some fine-scaled studies (response time better than 20 s). Several examples of accumulation curves for the largest fluxes are shown in Text S1.1 in the supporting information.

3.2. Measurement of Radon-222 Flux and Concentration

The accumulation chamber is also one of the preferred techniques used for the measurement of radon flux (Φ_{Rn}) [Cullen, 1946; Perrier *et al.*, 2009]. After placing the chamber on the ground, radon activity concentration A (expressed in Bq m⁻³) increases in the chamber with the accumulation time t . The radon flux, usually expressed in Bq m⁻² s⁻¹, is directly related to the slope at the origin of the radon accumulation curve ($dA/dt|_{t=0}$) according to [Ferry *et al.*, 2001; Richon *et al.*, 2005]

$$\Phi_{\text{Rn}} = \left. \frac{V dA}{S dt} \right|_{t=0}, \quad (2)$$

where V and S are the chamber volume and footprint area, respectively. The preparation at the surface for radon flux measurement is the same as for CO₂ flux measurement, and the most commonly used chambers had a volume of 0.0080 m³ and a footprint area of 0.092 m².

Lucas scintillation flasks (125 mL) were used to measure the radon concentration in the chamber [Lucas, 1957], and radon concentration was inferred from the photomultiplier count (CALEN™, Algade, France) obtained circa 3.5 h after the sampling [Perrier *et al.*, 2009; Girault *et al.*, 2009]. High-resolution accumulation curves could be obtained using sufficiently large numbers of samplings at different accumulation times. Measurement of high flux values required particular care, but reliable results could be achieved (Text S1.2 in the supporting information).

Two types of probes were used for continuous monitoring of radon concentration, both being set for hourly sampling/recording: Barasol™ probes (Algade, France) in 2008 and 2009 [Richon *et al.*, 2011] and second generation BMC2™ probes (Algade, France) in 2010. These are based on the detection of alpha particles by a silicon detector located 13 cm from the base of the probe behind a diffusion window. Their sensitivity is circa 50 Bq m⁻³, and intercomparison in the laboratory gave a dispersion of 3%, whereas the overall common uncertainty (associated with the specific measurement technique) was about 5%.

3.3. Temperature and Heat Flux Measurements

Robust temperature measurements were performed using Seabird™ probes (SBE39 Seabird™, Sea-Bird Electronics Inc., USA), designed for deep oceanography research. These probes were used both for temperature monitoring and heat flux estimations. Provisional heat flux measurements were made using the accumulation chamber method on the ground. As measurements were only performed at points with the highest CO₂ flux of GZ1 (CO₂ content was >90% in all soil-gas samples in GZ1), the CO₂ content in the air of

the chamber was taken as 100% for these heat flux calculations. The slope at the origin of the increase of the temperature (T in K) with time ($dT/dt|_{t=0}$) is related to the heat flux Φ_{heat} , expressed in W m^{-2} , according to

$$\Phi_{\text{heat}} = \rho_{\text{CO}_2} C_p^{\text{CO}_2} \frac{V}{S} \left. \frac{dT}{dt} \right|_{t=0}, \quad (3)$$

where T is the temperature, ρ_{CO_2} is the gaseous CO_2 density, $C_p^{\text{CO}_2}$ is the specific heat of CO_2 at constant pressure, and V and S are chamber volume and footprint area, respectively. The same experimental protocol was used for heat flux measurements as for CO_2 and radon flux measurements, with chambers of 0.0083 m^3 volume and 0.093 m^2 footprint area.

Seabird™ probes recorded at 30 s intervals. The sensitivity of the Seabird™ probes is given to be $10^{-4} \text{ }^\circ\text{C}$ by the manufacturer, and specific experiments showed that these were intercalibrated to an accuracy better than $3.5 \times 10^{-3} \text{ }^\circ\text{C}$. Punctual uncertainty (associated with a measured point and statistically independent from measurement to measurement) ranged from 2.5% for small heat fluxes to 30% for high heat fluxes.

3.4. Measurement of Effective Radium Concentration

The source of radon is related to the radium concentration (C_{Ra}) of rocks and soils [Sakoda *et al.*, 2011]. However, only a fraction of the radium atoms are able to release radon atoms in the porous media of the rock or soil. This fraction is the emanation E , defined as the probability that a radium atom produces a radon atom in the pore space [Tanner, 1964; Nazaroff, 1992]. Therefore, the relevant quantity for radon production is the effective radium concentration (EC_{Ra}), expressed in Bq kg^{-1} [Stoulos *et al.*, 2004]. As it is impossible to know a priori the EC_{Ra} of a given soil or rock, it was measured in the laboratory on 85 soil samples collected in the gas zones.

The measurement method is a radon accumulation technique [Stoulos *et al.*, 2003], already described elsewhere [Girault *et al.*, 2011a; Girault and Perrier, 2012] and detailed in Text S1.6 in the supporting information. Statistical uncertainty ranges from 8–10%, for EC_{Ra} values higher than 50 Bq kg^{-1} , to 30%, for EC_{Ra} values smaller than 0.2 Bq kg^{-1} , and to these, an additional uncertainty of 8% needs to be added quadratically to obtain the punctual uncertainty of each measurement [Girault and Perrier, 2012].

3.5. Measurement of Carbon Isotopic Ratio

Sampling of gas was performed using accumulation chambers and glass tubes fitted with valves. A chamber, previously pierced and fitted with a rubber plug, was placed on the ground as for radon flux measurements. After a minimum accumulation time of 20 min, an evacuated tube was inserted through the chamber at the plug location, and after about 10 min of ensuring gas homogenization inside the chamber, sampling was performed with the tube. Gas samples taken on the ground of the gas zones were analyzed for molecular composition, giving $\delta^{13}\text{C}$, using the method described by Evans *et al.* [2008]. A description of the protocol is described in Text S1.7 in the supporting information.

3.6. Measurement of Helium Isotopic Ratio

Sampling of gas was performed using accumulation chambers and preevacuated stainless steel tubes fitted with valves. The pierced chamber equipped with the tube was put on the ground as for radon flux measurements, having been previously depressurized using a handheld pump. After a minimum accumulation time of 30 min, the valve was opened, and the accumulated gas was drawn into the sampling tube. After about 10 min of ensuring gas homogenization inside the chamber and the tube, the valve was closed, capturing the sample. Gas samples were analyzed for helium isotopic composition using the method described in Text S1.8 in the supporting information. The helium isotope ratio R/R_A is defined by the $^4\text{He}/^3\text{He}$ ratio of the sample divided by the $^4\text{He}/^3\text{He}$ ratio of the atmosphere (1.39×10^{-6}).

4. Summary of Results

4.1. Assessment of Uncertainties on Gas Flux Measurements

Two separate contributions to the total uncertainty are considered for the experimental techniques in this paper: punctual uncertainty, which is associated with a measured point and statistically independent from measurement to measurement, and overall common uncertainty, which is associated with the specific measurement technique. The absolute total uncertainty corresponds to the quadratic sum of these two

Table 1. Summary of the Sources of Uncertainties in the Measurement of CO₂ and Radon Flux

Uncertainty Source	CO ₂ Flux	Radon Flux
Main punctual uncertainties		
Determination of slope of accumulation curve	0.5–30%	<1%
Counting statistics and dilution correction	-	5–30%
Intercalibrations and systematic effects evaluated experimentally (see supporting information)	5–20%	5–20%
Total punctual uncertainty	5–40%	8–35%
Overall common uncertainty		
Absolute calibration	5%	5%

contributions; the relative total uncertainty is defined as the absolute total uncertainty divided by the (mean) measurement value. The details of the different sources of uncertainty on CO₂ and radon flux measurements are summarized in Table 1.

For CO₂ flux measurement, the punctual uncertainty mainly came from the uncertainty of the slope of the accumulation curve and ranged from 0.5 to 30% depending on the point. As illustrated in Text S1.1 in the supporting information, various types of accumulation curves were observed, and the value of the slope depended on the particular section used to make the estimation. This uncertainty was estimated by changing the time window [Girault, 2011]. Other sources of uncertainty, such as the determination of the size of the chamber or the ruggedness of the soil, were found negligible compared with the uncertainty from the accumulation curve. To account for systematic effects, an additional effective punctual uncertainty in CO₂ flux measurements was set in this paper, as elaborated by the large number of systematic experiments (total of 326 CO₂ flux measurements) detailed in Text S1.3 in the supporting information, ranging from 5% for small CO₂ flux (<100 g m⁻² d⁻¹) to 20% for high CO₂ flux (>3000 g m⁻² d⁻¹), with a smooth transition from small to high fluxes. Intercalibration of CO₂ sensors was checked several times in the laboratory from 2007 to 2011. Differences were found, ranging over 4–7%. The absolute calibration factor of the CO₂ sensor used for intercalibration experiments (5%) was taken into account as the only source of overall common uncertainty. The relative total uncertainty is plotted as a function of the CO₂ flux in Figure 3 for the four sensor types and the whole data set obtained in the SBHS. The Vaisala™ 1% sensor was generally more accurate than the Testo™ sensors for small CO₂ fluxes, whereas the Vaisala™ 20%, able to measure the highest CO₂ fluxes, gave similar uncertainties as the Airwatch™ sensors (Figure 3).

For radon flux measurement, the punctual uncertainty was dominated by the counting statistics and by the dilution correction after the sampling and ranged from 5 to 30%. The other sources of punctual uncertainties, such as the precision of the accumulation time effectively recorded, ruggedness of the soil, and dispersion of the calibration factor of scintillation flasks [Girault, 2011], are negligible in comparison. As for CO₂ flux, various experiments (total of 357 radon flux measurements) were conducted in the field to account for systematic effects (Text S1.3 in the supporting information), and an additional effective punctual uncertainty ranging from 5% for small radon fluxes (<100 × 10⁻³ Bq m⁻² s⁻¹) to 20% for high radon fluxes (>3000 × 10⁻³ Bq m⁻² s⁻¹) was incorporated. In addition, to compare with other measurements, an overall common uncertainty (absolute calibration) of 5% has to be added quadratically. The relative total uncertainty is plotted as a function of the radon flux value in Figure 4 for the whole data set obtained in the SBHS. In general, the measurement of radon

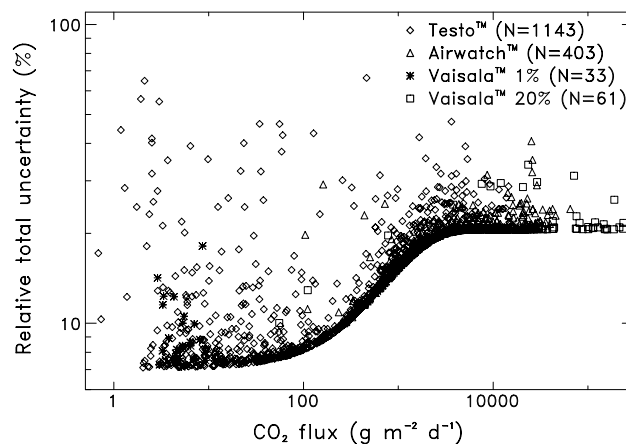


Figure 3. Relative total uncertainty in CO₂ flux measurement expressed in percent as a function of the given mean CO₂ flux separately for each type of sensor. The entire data set obtained in the SBHS is plotted.

measurements (total of 357 radon flux measurements) were conducted in the field to account for systematic effects (Text S1.3 in the supporting information), and an additional effective punctual uncertainty ranging from 5% for small radon fluxes (<100 × 10⁻³ Bq m⁻² s⁻¹) to 20% for high radon fluxes (>3000 × 10⁻³ Bq m⁻² s⁻¹) was incorporated. In addition, to compare with other measurements, an overall common uncertainty (absolute calibration) of 5% has to be added quadratically. The relative total uncertainty is plotted as a function of the radon flux value in Figure 4 for the whole data set obtained in the SBHS. In general, the measurement of radon

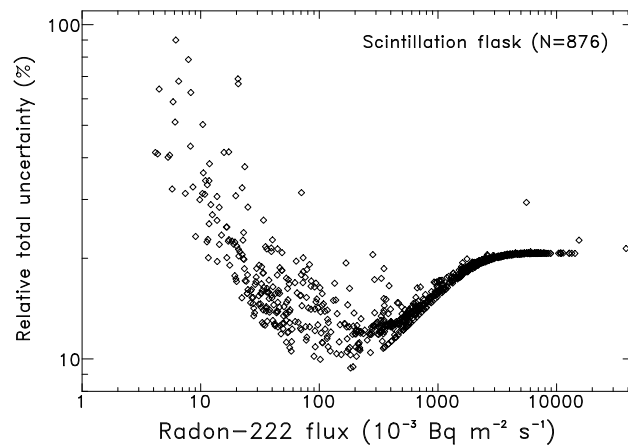


Figure 4. Relative total uncertainty in radon flux measurement expressed in percent as a function of the given mean radon flux. The entire data set obtained in the SBHS is plotted.

flux appeared more accurate for high flux and less accurate for small flux (Figure 4), whereas the reverse situation was observed for the measurement of CO_2 flux (Figure 3).

In the figures presented in this paper, error bars of CO_2 and radon fluxes correspond to the total punctual uncertainty at one standard deviation confidence level (68%). As we have a minimum of two measured values of flux per point, error bars correspond to the standard deviation divided by the square root of the number of measurements at the considered point. In addition, all quoted averages in the text are geometric means, unless stated otherwise.

4.2. CO_2 and Radon Fluxes

Results of the CO_2 and radon flux measurements carried out in GZ1–GZ5 and background areas during the dry winter seasons of the 2007–2011 period are summarized in Table 2. Results of monsoon season (summer) measurements are also shown for GZ1 and GZ3. For the background areas, each gas zone individually, and the gas zones aggregated together, the CO_2 and radon flux results are summarized in terms of number of measurements, range of measured values, and arithmetic and geometric means.

Along the background profile GPX (Figure 5), for which there is a significant number (37) of data points, higher background CO_2 and radon fluxes are observed on organic-rich soils (terraces) than on sandy or dry soils (debris cone). Similar flux differences occurred in all other background profiles [Girault, 2011] (Text S2.1 in the supporting information). Interestingly, the CO_2 flux decreased toward the northeast by $1.0 \pm 0.3 \text{ g m}^{-2} \text{ d}^{-1} / 100 \text{ m}$ for the GZ5D and GZ5E background profiles. With regard to all the background areas, the average fluxes of $8.6 \pm 0.1 \text{ g m}^{-2} \text{ d}^{-1}$ for CO_2 and $(26.9 \pm 0.5) \times 10^{-3} \text{ Bq m}^{-2} \text{ s}^{-1}$ for radon are similar to the international continental averages of circa $10 \text{ g m}^{-2} \text{ d}^{-1}$ for CO_2 flux [e.g., Angell et al., 2001; Awasthi et al., 2005; Reth et al., 2005] and circa $22 \times 10^{-3} \text{ Bq m}^{-2} \text{ s}^{-1}$ for radon flux [e.g., Schery et al., 1989; Nazaroff, 1992; Szegvary et al., 2007].

For GZ1, the main measurements were performed along the measurement profile shown in Figure 6. This profile was 27 m long from southwest to northeast and followed the recesses of the two cavities 1B and 2, located in the area without vegetation between the points 13.4 and 22.5 m. The central part of the profile, between 9 and 25 m, was characterized by extremely high CO_2 and radon fluxes (maxima $236,000 \text{ g m}^{-2} \text{ d}^{-1}$ and $38,500 \times 10^{-3} \text{ Bq m}^{-2} \text{ s}^{-1}$, respectively), the largest values recorded in these gas zones. Three other profiles were carried out, from the recess of cavity 1B to the area without vegetation toward east (A) and toward south (B), and of circular shape around the cavities and the area without vegetation (C) (Figure 6). Along these profiles, the ranges of variation of CO_2 and radon fluxes (Table 2) were particularly large (Figure 7), with averages greater than $30,500 \text{ g m}^{-2} \text{ d}^{-1}$ and $10,800 \times 10^{-3} \text{ Bq m}^{-2} \text{ s}^{-1}$, respectively. However, the end parts of all these four profiles were characterized by smaller CO_2 and radon fluxes which are of the same order of magnitude as the background fluxes (Figures 6 and 7). Data collected during the monsoon showed no significant changes, to the first order, as compared with the dry winter season values (Figure 6), as observed previously in GZ3 [Girault et al., 2009].

The CO_2 and radon fluxes for GZ2 (Figure 8) were carried out tracing the recess of the cavity. There, fluxes show the highest averages of the five gas zones measured, i.e., $3680 \pm 220 \text{ g m}^{-2} \text{ d}^{-1}$ for CO_2 and $(1550 \pm 40) \times 10^{-3} \text{ Bq m}^{-2} \text{ s}^{-1}$ for radon, although the maximum fluxes of $34,000 \text{ g m}^{-2} \text{ d}^{-1}$ for CO_2 and $7200 \times 10^{-3} \text{ Bq m}^{-2} \text{ s}^{-1}$ for radon are smaller than those of GZ1.

Table 2. Summary of the Results of CO₂ and Radon Flux Measurements, Separately in the Background Areas, in the Five Gas Zones and in the Aggregated Gas Zones of the SBHS in the Dry Season^a

Period of Measurement	Dry Season					Monsoon			
	Background	All Gas Zones	Gas Zone 1	Gas Zone 2	Gas Zone 3	Gas Zone 4	Gas Zone 5	Gas Zone 1	Gas Zone 3
Estimated surface of the site (m ²)		21,550	500	150	5400	2000	13,500		
CO₂ flux (g m⁻² d⁻¹)									
Number of measurements	206	1108	359	68	580 ^b	51	50	19	115 ^b
Number of measurement points	181	341	96	20	139	39	47	9	53
Range min-max	0.7–129	2.0–236,000	2.5–236,000	210–34,100	2.0–19,000	3.2–6230	3.7–580	1660–31,300	11–14,500
Arithmetic mean	13.1 ± 1.2	4611 ± 794	10,660 ± 2240	5860 ± 1060	1960 ± 300	424 ± 152	74 ± 14	10,160 ± 3260	1050 ± 220
Geometric mean	8.6 ± 0.1	418 ± 5	1026 ± 21	3679 ± 220	733 ± 19	79 ± 2	34 ± 1	6720 ± 230	433 ± 18
Estimated total discharge (t d ⁻¹)		5.93 ± 1.56 ^c	1.35 ± 0.28	0.29 ± 0.07	2.52 ± 0.53	0.27 ± 0.06	0.33 ± 0.07		
Estimated total discharge (mol s ⁻¹)		1.56 ± 0.41 ^c	0.35 ± 0.07	0.08 ± 0.02	0.66 ± 0.14	0.07 ± 0.02	0.09 ± 0.02		
Estimated surface of flux > 1000 g m ⁻² d ⁻¹ (m ²)		1050 ± 220	111 ± 22	58 ± 12	840 ± 170	42 ± 12	0		
Estimated surface of flux > 500 g m ⁻² d ⁻¹ (m ²)		1670 ± 360	131 ± 27	66 ± 13	1350 ± 280	120 ± 27	4 ± 5		
Radon flux (10⁻³ Bq m⁻² s⁻¹)									
Number of measurements	73	446	149	35	203 ^b	42	17	9	34 ^b
Number of measurement points	73	260	97	20	88	38	17	9	30
Range min-max	4.2–119	1.2–38,500	4.5–38,500	97–7220	1.2–10,400	8.2–2390	21–220	864–7030	6.5–3370
Arithmetic mean	33.0 ± 2.5	1300 ± 152	2110 ± 329	2310 ± 410	790 ± 140	290 ± 90	85 ± 13	2920 ± 650	660 ± 170
Geometric mean	26.9 ± 0.5	258.5 ± 0.2	332 ± 6	1548 ± 35	315 ± 7	83 ± 2	72 ± 2	2450 ± 25	259 ± 13
Estimated total discharge (MBq d ⁻¹)		140 ± 29	19.1 ± 3.9	10.5 ± 2.3	90 ± 18	12.3 ± 2.5	8.1 ± 1.7		
Estimated total discharge (Bq s ⁻¹)		1618 ± 333	221 ± 46	121 ± 27	1040 ± 212	143 ± 29	93 ± 19		
Estimated surface of flux > 500 × 10 ⁻³ Bq m ⁻² s ⁻¹ (m ²)		760 ± 160	62 ± 13	57 ± 12	610 ± 130	27 ± 7	0		
Estimated surface of flux > 250 × 10 ⁻³ Bq m ⁻² s ⁻¹ (m ²)		1600 ± 330	95 ± 19	66 ± 13	1300 ± 260	133 ± 38	0		
Radon-CO₂ correlation									
Number of averaged values	73	240	92	20	82	29	17	9	30
Correlation coefficient	0.76 ± 0.02	0.86 ± 0.02	0.90 ± 0.02	0.96 ± 0.02	0.94 ± 0.02	0.89 ± 0.07	0.90 ± 0.01	0.62 ± 0.02	0.85 ± 0.04

^aResults of GZ1 and GZ3 obtained during monsoon are also included.

^bIn GZ3 during dry season (monsoon), 417 (100) CO₂ flux and 118 (27) radon flux measurements are from Girault et al. [2009].

^cThe estimated CO₂ degassing from the cavity in GZ4, 1.17 ± 0.55 t d⁻¹ or 0.31 ± 0.14 mol s⁻¹, has also been included (Text S2.2 in the supporting information).

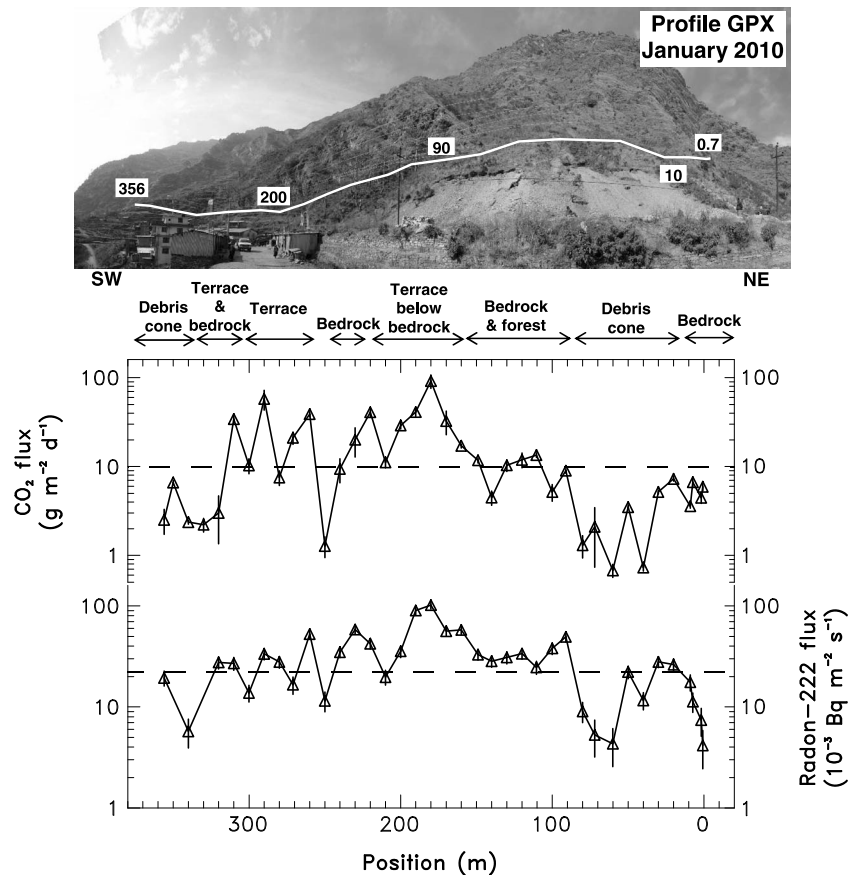


Figure 5. CO₂ and radon fluxes obtained in background profile GPX. The profile is located on the west bank of the Trisuli River (Figure 1). From top to bottom: photograph of the gas profile; results of CO₂ and radon fluxes as a function of the position along the profile. The dashed lines correspond to the mean background CO₂ flux (10 g m⁻² d⁻¹) and radon flux (22 × 10⁻³ Bq m⁻² s⁻¹) commonly accepted for continental background (see text).

Several profiles were monitored for CO₂ flux (seven) and radon flux (four) in GZ3 along the road. The main profile, 660 m long SW-NE, showed high CO₂ and radon fluxes in its central part, between points 33 m and 0 m (Figure 9), where averages reached 1010 ± 63 g m⁻² d⁻¹ and (415 ± 19) × 10⁻³ Bq m⁻² s⁻¹, respectively. These data are similar to the fluxes measured along the other horizontal profiles (along the road). Furthermore, numerous points were also measured during the monsoon along the main profile (Figure 9), thus adding a significant number of measurements to the previous study [Girault et al., 2009]. Again, no significant changes (to first order) were noticed compared with the dry winter season data. However, anomalously high CO₂ and radon fluxes, >12,000 g m⁻² d⁻¹ and > 6500 × 10⁻³ Bq m⁻² s⁻¹, respectively, were measured along a perpendicular profile, 103 m long (45 m vertically) and crossing the road (Figure 10). Taking into account all profiles, average CO₂ and radon fluxes were 733 ± 19 g m⁻² d⁻¹ and (315 ± 7) × 10⁻³ Bq m⁻² s⁻¹, respectively.

Measurements in GZ4 were divided into two groups, outside and inside the cavity (Figure 11). Four profiles (A–D) were conducted outside the cavity: profiles A and C were horizontal and parallel, profile B was perpendicular to profiles A and C beginning at the cavity wall and turning toward the river, and profile D refined the region where profiles B and C crossed. The highest fluxes, 6200 g m⁻² d⁻¹ for CO₂ and 2400 × 10⁻³ Bq m⁻² s⁻¹ for radon, were obtained in a small area (circa 5 m × 5 m) in profiles B and C. Measurements from points 0 m to 10 m of profile B are potentially influenced by the high concentrations in the cavity and should be interpreted in this context.

Three measurement profiles (A–C) were performed in GZ5 (Figure 12). Profiles A and C showed the same trend of an increase in CO₂ flux from northeast to southwest; this observation might be due to the presence of a hot spring near the point 137 m of profile A. In general, CO₂ and radon fluxes were quite small with

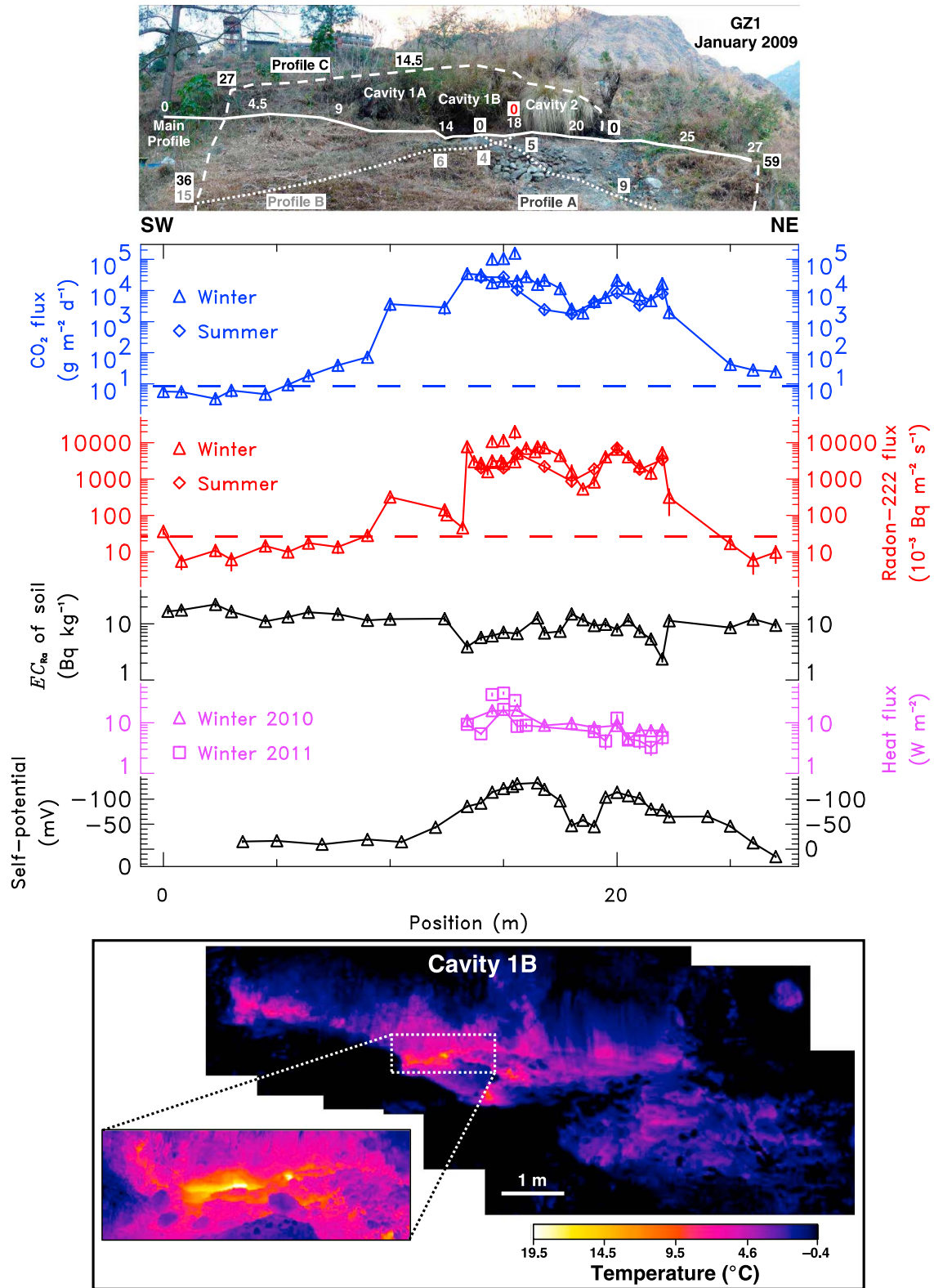


Figure 6. Results of the main profile of GZ1. From top to bottom: photograph of the site; results of CO₂ flux, radon flux, EC_{Ra} of soil samples, heat flux, and SP data as a function of the position along the profile; and thermal infrared image of cavity 1B taken in January 2011. The horizontal dashed lines correspond to the average background CO₂ and radon fluxes obtained in the SBHS.

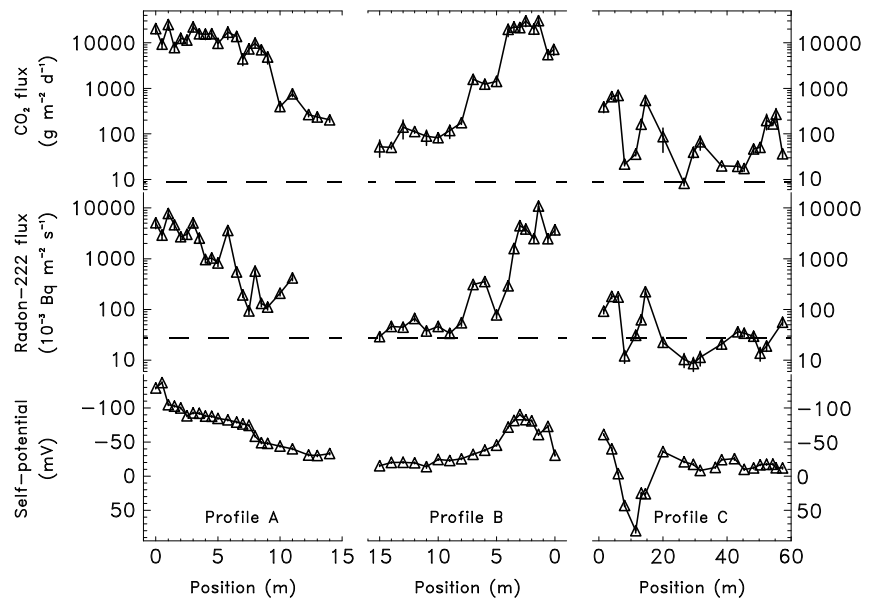


Figure 7. CO₂ flux, radon flux, and SP measurement results of the three auxiliary profiles in GZ1 as a function of their respective position. See Figure 6 for the location of these profiles. The dashed lines correspond to the average background CO₂ and radon fluxes obtained in the SBHS.

averages of $34 \pm 1 \text{ g m}^{-2} \text{ d}^{-1}$ and $(72 \pm 2) \times 10^{-3} \text{ Bq m}^{-2} \text{ s}^{-1}$, respectively, although significantly higher than the background fluxes.

4.3. Soil Effective Radium Concentration

At each measurement point of the main GZ1 profile (Figure 6), soil was sampled, and its effective radium concentration (EC_{Ra}) was determined in the laboratory. The values of EC_{Ra} appear similar with average (range, min-max) 9.7 ± 0.2 (2.4–22) Bq kg^{-1} . However, in the zone without vegetation and with the highest CO₂ and radon fluxes, EC_{Ra} values were systematically smaller, by a factor of 1.7 ± 0.2 , than the rest of the profile, changing abruptly (close to an order of magnitude) at the boundaries of this zone. This is, to our knowledge, the first time that such a depletion effect of effective radium concentration has been reported in the presence of large CO₂ discharge.

EC_{Ra} values of soil samples in GZ2 (Figure 8), $8.8 \pm 0.2 \text{ Bq kg}^{-1}$ on average, are similar to the values obtained with soil samples in GZ1. As in GZ1, EC_{Ra} values in GZ2 were higher outside the largest degassing zone, although by a smaller factor (1.3 ± 0.2) and with a less well defined change (factor of 2.3 ± 0.2) in EC_{Ra} at the boundaries of this highest degassing zone (at points 1 and 11 m).

EC_{Ra} values of soil samples collected over the main GZ3 profile (Figure 9) varied from 4.4 to 14 Bq kg^{-1} with a mean of $7.7 \pm 0.1 \text{ Bq kg}^{-1}$. EC_{Ra} values were reasonably uniform over this profile. However, smaller EC_{Ra} values were observed at the sides of the large degassing area in this site, and the highest EC_{Ra} value was obtained at point 22 m, which had the smallest CO₂ flux. In addition, soil was sampled 50 cm from the ancient cavity (Figure 10) and gave a comparable EC_{Ra} value of $9.0 \pm 0.5 \text{ Bq kg}^{-1}$.

Two sets of EC_{Ra} values were determined with soil samples collected in GZ4. Soil samples of two points outside the cavity having the highest radon flux in GZ4 yielded a mean EC_{Ra} value of $28.0 \pm 0.3 \text{ Bq kg}^{-1}$. This mean was approximately twice as high as for values measured in the other gas zones. EC_{Ra} was also measured with one soil sample from inside the cavity, yielding a value of $21.9 \pm 1.8 \text{ Bq kg}^{-1}$, similar to, albeit slightly smaller than, the values of samples outside the cavity.

4.4. Gas Temperature, Concentrations, and Isotope Ratios

The gas temperature, concentrations, carbon isotopic ratios ($\delta^{13}\text{C}$), and helium isotopic ratios (R/R_A) are summarized in Table 3. An overview of the temperature, pressure, and radon concentration time series measured at circa 70 cm depth and rainfall is available in Text S3.2 in the supporting information.

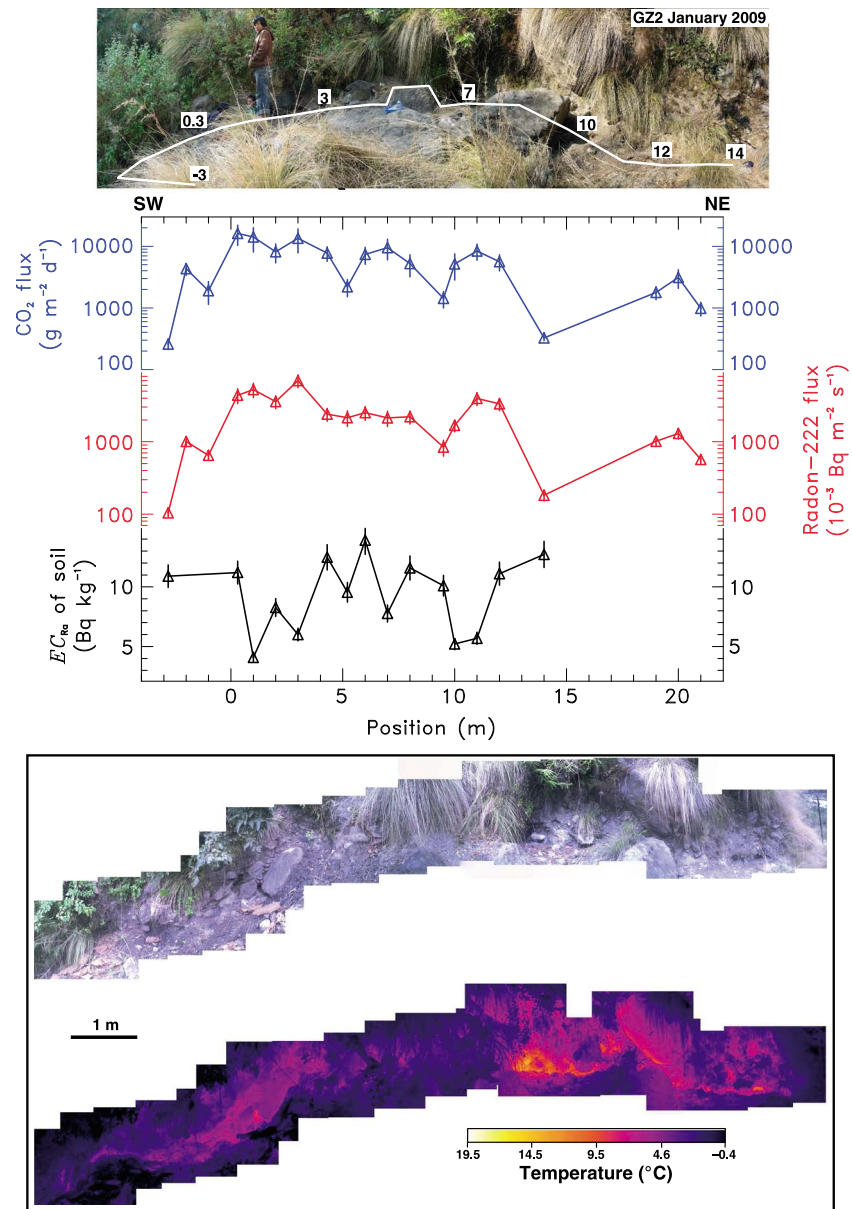


Figure 8. Results of GZ2. From top to bottom: photograph of the site; results of CO₂ flux, radon flux, and EC_{Ra} of soil samples as a function of the position along the profile; and thermal infrared image taken in January 2011. The horizontal dashed lines correspond to the average background CO₂ and radon fluxes obtained in the SBHS.

In GZ1, gas temperature and concentrations were measured in the cavities and in the places without vegetation, both in the soil and in the air. Mean gas temperatures reached 28.8°C and 24.7°C in the soil and in the air of cavity 1B, respectively. The CO₂ concentration in the air of cavities 1A and 1B was greater than 60%, whereas it was only circa 4% in the air of cavity 2. Radon concentration was measured at 70 cm depth in the soil of cavity 1B using two closely spaced PVC tubes (A and B) [Richon *et al.*, 2011] and at 1 m depth in the soil of the zone without vegetation, outside the cavities, using two metallic tubes. Average concentrations varied from 39×10^3 to 49×10^3 Bq m⁻³. The five CO₂ concentration measurements on the ground of cavity 1B exceeded 91% with average $\delta^{13}\text{C} = -0.8 \pm 0.1\text{‰}$ (including three 2007 values from Perrier *et al.* [2009]). Two additional gas samples were taken on the ground of cavity 1B for helium analysis: these results were similar to within circa 2%, with an average helium concentration of 76.4 ± 1.1 ppm, with $R/R_A < 0.05$ for both samples.

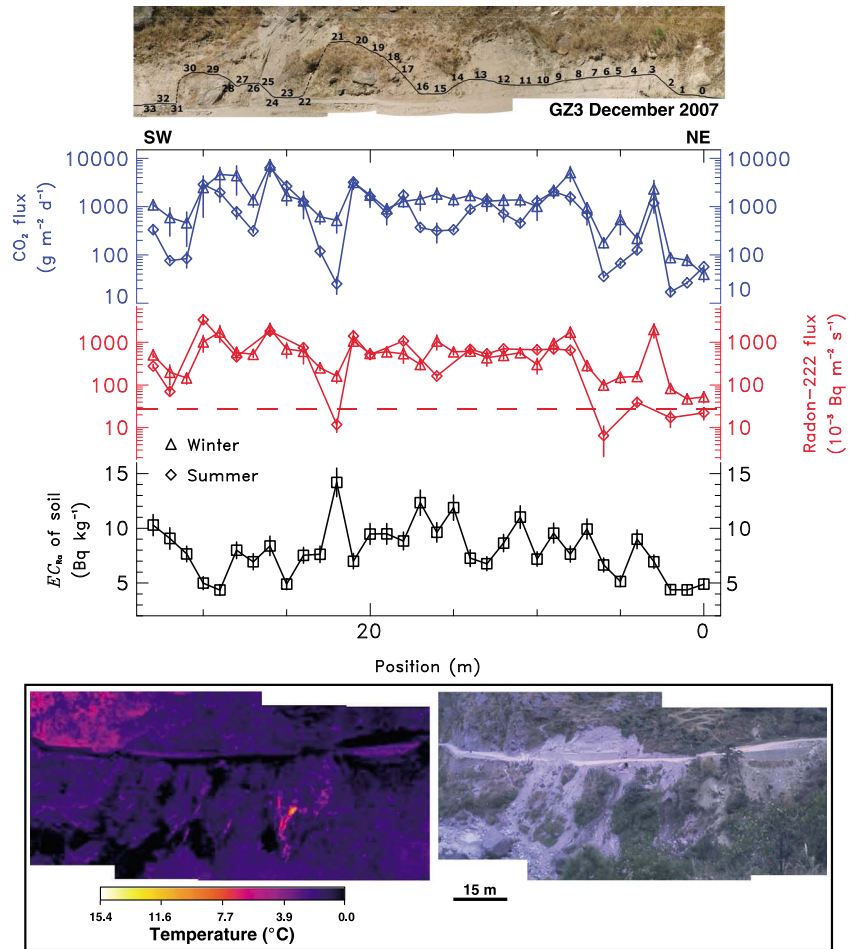


Figure 9. Results of the main profile of GZ3 (data from 2007 to 2010). From top to bottom: photograph of the central site of the gas zone taken in dry winter season [Girault et al., 2009]; results of CO₂ flux, radon flux, and EC_{Ra} of soil samples as a function of the position along the profile; and thermal infrared image of the entire site taken in January 2011 from the opposite bank. The horizontal dashed lines correspond to the average background CO₂ and radon fluxes obtained in the SBHS.

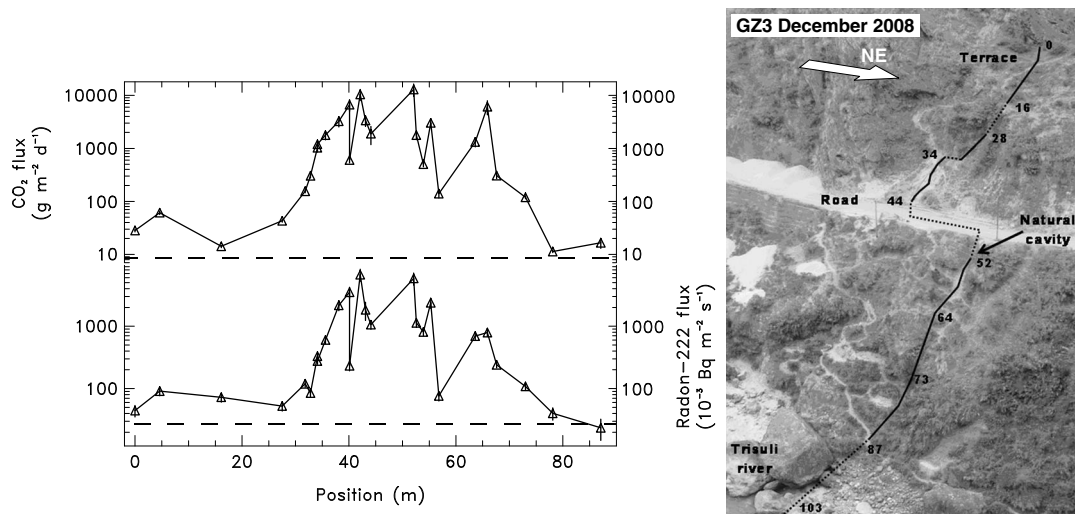


Figure 10. Results of the vertical profile in GZ3. A photograph of the profile (taken in 2008) is presented on the right where the location of the ancient cavity is indicated. Results of CO₂ and radon flux measurements are shown on the left as a function of the position along the profile. The horizontal dashed lines correspond to the average background CO₂ and radon fluxes obtained in the SBHS.

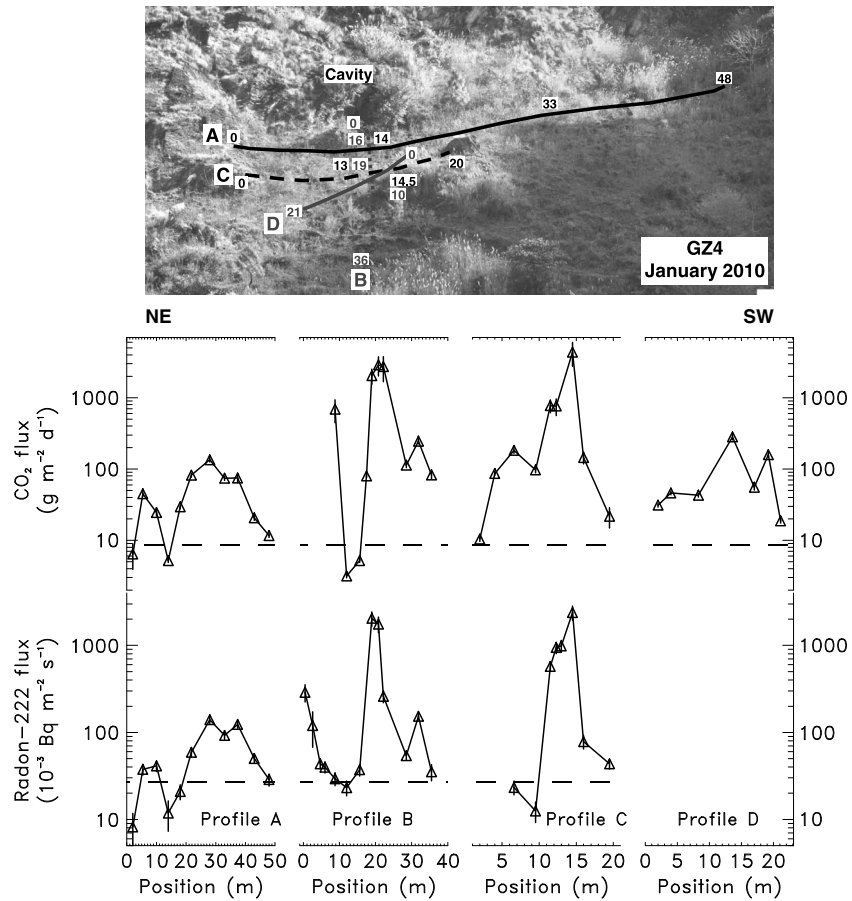


Figure 11. Results of the gas measurement profiles A, B, C, and D in GZ4. The photograph (taken in 2010) shows locations of the four profiles and the cavity. The horizontal dashed lines correspond to the average background CO₂ and radon fluxes obtained in the SBHS.

In GZ2, gas temperature and radon concentration were measured at 70 cm depth in the soil of the recess of the cavity using a PVC tube [Richon *et al.*, 2011]: mean values reached 25.2°C and circa $47 \times 10^3 \text{ Bq m}^{-3}$, respectively. The average CO₂ concentration exceeded 97%, the highest measured in any of the gas zones, with average $\delta^{13}\text{C} = -1.0 \pm 0.2\text{‰}$.

In GZ3, gas temperature and radon concentration were measured over 1 year in the air 2 cm above the ground inside the ancient cavity [Richon *et al.*, 2011] (Figure 10) and over a 12 h period at 70 cm depth in the soil of the main profile (point 27 m in Figure 9), giving average values of 21.4°C and circa $77 \times 10^3 \text{ Bq m}^{-3}$ in the cavity, respectively, compared to 10.3°C and circa $74 \times 10^3 \text{ Bq m}^{-3}$ in the soil in GZ3 (measured in January 2011). Also, air CO₂ concentration was measured once in the cavity (88%) and once on the ground in the main profile (80%) yielding $\delta^{13}\text{C} = -0.5 \pm 0.1\text{‰}$. Sampling for helium isotope ratios was not possible during the period of road and bridge construction.

In GZ4, the soil radon concentration was measured over a 12 h period at 70 cm depth in the soil of the point where the highest radon flux was recorded outside the cavity, giving an average of circa $64 \times 10^3 \text{ Bq m}^{-3}$. In addition, the soil CO₂ concentration on the ground was measured (30%), yielding $\delta^{13}\text{C} = -1.0 \pm 0.1\text{‰}$. In the cavity of GZ4 where the mean gas temperature was 21.3°C, CO₂ and radon concentrations were measured: 32% for CO₂ and circa $9 \times 10^3 \text{ Bq m}^{-3}$ for radon [Richon *et al.*, 2011]. In addition, a tube was used to sample the air of the cavity, at circa 30 cm height. Although this sample was mixed with ambient air, a relatively high CO₂ concentration of circa 9% was obtained, as well as $\delta^{13}\text{C} = -1.7 \pm 0.1\text{‰}$, which is smaller than in the soil-gas samples.

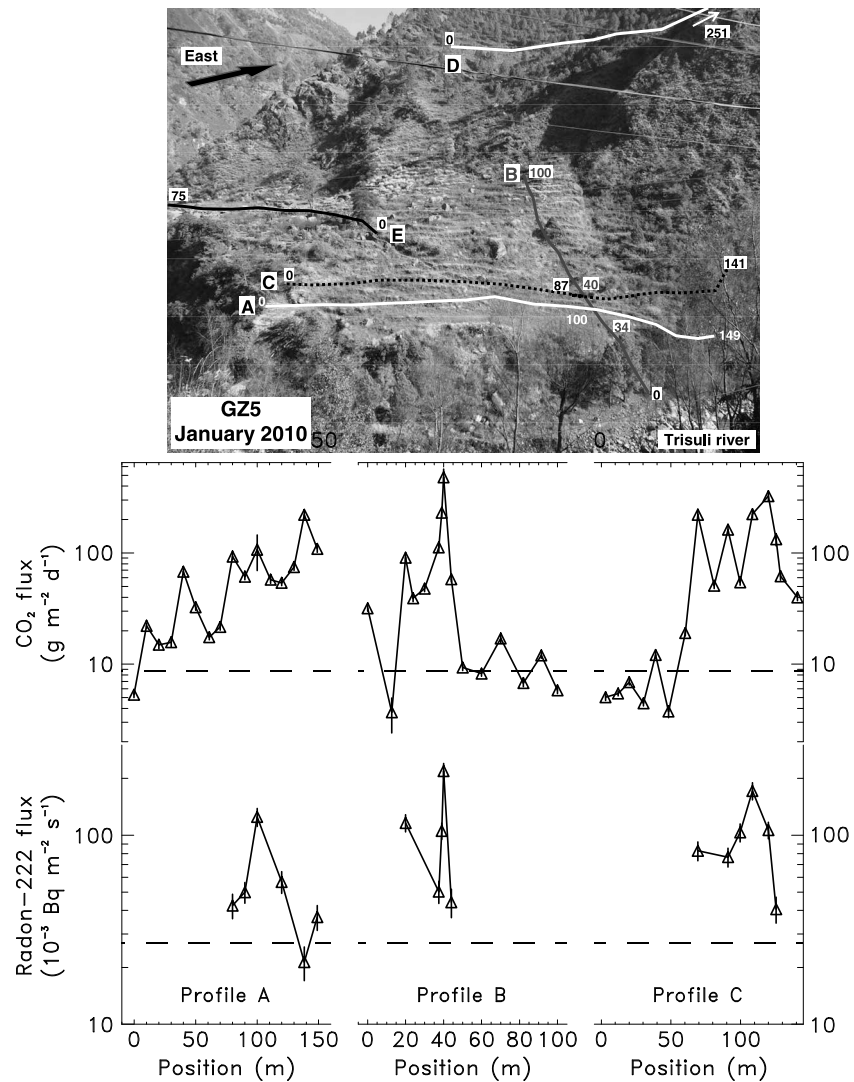


Figure 12. Results of the gas measurement profiles A, B, and C in GZ5. From top to bottom: photograph (taken in 2010) of these three profiles together with two background profiles (GZ5D and GZ5E); CO₂ and radon flux results as a function of the position for the three profiles of the gas zone. The horizontal dashed lines correspond to the average background CO₂ and radon fluxes obtained in the SBHS.

In summary, radon concentration appears similar in GZ1 and GZ2 (circa $40 \times 10^3 \text{ Bq m}^{-3}$) located close to the main hot springs, but significantly higher in GZ3 and GZ4 (circa $70 \times 10^3 \text{ Bq m}^{-3}$) located 500 m from the main hot springs. This feature of the SBHS is interpreted in the companion paper [Girault and Perrier, 2014].

4.5. Other Measurements

The thermal infrared imaging of GZ1 (Figure 6) indicated that the region of highest temperature ($>14.5^\circ\text{C}$) was located in cavity 1B. The enlargement in Figure 6 illustrates the region of whistling CO₂ points, with their associated major temperature anomaly reaching above 39°C . Heat flux measurements were carried out in the central area of the main GZ1 profile. Results obtained in winters 2010 and 2011, compatible within uncertainties, are presented in Figure 6. The values were relatively large, with an average of $13 \pm 3 \text{ W m}^{-2}$ in winter 2011. The signatures of the two cavities are clear in Figure 6, characterized by an increase of the heat flux at points 15 and 20 m.

Table 3. Summary of CO₂ and Radon Concentration and Results of Carbon and Helium Isotopic Ratios in the Main Gas Zones of the SBHS

Measurement Location	Air				Ground Surface				Soil (circa 70 cm depth)							
	GZ1 Cav. 1A	GZ1 Cav. 1B	GZ1 Cav. 2	GZ1	GZ3 Cav.	GZ4 Cav.	GZ1	GZ2	GZ3	GZ4	GZ1 Cav. 1B, A	GZ1 Cav. 1B, B	GZ1 Soil	GZ2	GZ3	GZ4
Gas temperature																
Mean					21.4 ± 1.9 ^a	21.3 ± 1.8 ^a										
Min/Max (°C)	14.2/24.7	10.5/20.3	18.0/23.2 ^a	17.0/24.6 ^a												
CO₂ and radon concentrations																
Max CO ₂ (%)	>60	>60	4	32												
Mean radon (10 ³ Bq m ⁻³)					77.4 ± 1.3	9 ± 7 ^a										
Min/Max radon (10 ³ Bq m ⁻³)					71.4/82.8	2/12 ^a										
Carbon isotopic ratio analyses																
Number of measurements					1	1	5	2	1	1						
Period of sampling					2010	2010	2007 and 2011	2010 and 2011	2007	2011						
Mean CO ₂ content (%)					87.5 ± 1.0	8.7 ± 0.5	92.3 ± 0.4	97.5 ± 1.0	79.6 ± 1.0	30.0 ± 0.1						
(Min/Max)							(91.6/92.9)									
Mean δ ¹³ C of gaseous CO ₂ (‰)					n.m.	-1.7 ± 0.1	-0.8 ± 0.1	-1.0 ± 0.2	-0.5 ± 0.1	-1.0 ± 0.1						
(Min/Max)																
Helium isotopic ratio analyses																
Number of measurements							2									
Mean He content (ppm)							76.4 ± 1.1									
(Min/Max)							(75.6/77.1)									
Ratio R/R _A							<0.05									

^aAfter Richon et al. [2011].

^bGas temperature was measured in the soil at three distinct locations in GZ1 (Text S3.2 in the supporting information): in the area without vegetation, 2 m from cavity 2 (GZ1C), where radon concentration was monitored (25.2 ± 2.0°C) and below the boulder (GZ1E) visible in Figure 6 (23.9 ± 3.3°C) and in the area with vegetation, on profile C 10 m from cavity 2 (21.6 ± 3.5°C). n.m.: not measured.

The self-potential (SP) distribution is an important feature of GZ1 and provides additional information of the fluid circulation near the surface [Byrdina *et al.*, 2009; Revil *et al.*, 2012]. Therefore, SP results for the main profile in GZ1 are also shown in Figure 6. The two cavities, 1B and 2, yielded anomalies of circa -130 mV and -110 mV, respectively, and are clearly evident as the maxima in the SP data in Figure 6, separated by a minimum of circa -50 mV. When looking at the other profiles in GZ1 (Figure 7), SP anomalies here reached -137 mV, in agreement with previous results obtained in December 2007 [Byrdina *et al.*, 2009]. The long-term temporal stability of the SP signature is a nontrivial confirmation of the stability of the system despite the presence of large meteorological perturbations and a confirmation of the model presented previously [Byrdina *et al.*, 2009]. The trends in SP values tended to be smoother than the trends of the CO₂ and radon fluxes, in particular in profile B (Figure 7). Compared with the previous experiment [Byrdina *et al.*, 2009], these new data allow a more precise comparison between SP and CO₂ flux, both measured with precision at the same point. A significant correlation is confirmed between CO₂ fluxes and SP anomalies in GZ1 (Text S3.1 in the supporting information).

The thermal infrared imaging of GZ2 (Figure 8) revealed two remarkable warm spots, reaching more than 15°C , located in the recess of the cavity. These warm spots correspond to the areas of sulphur and sulphate deposits (with warm soil and gas temperature in the soil above 25°C).

In 2010, after measurements were performed along the main profile of GZ3, a long wall (30 m) was built as part of the new road, creating an artificial modification to the degassing regime (optical image in Figure 9). While the thermal anomalies along the road were difficult to observe after the construction of the wall, small warm spots became apparent at the base of the wall, suggesting continuation of degassing at that location. It was however impossible to access to the highest warm spots (temperature $>15^{\circ}\text{C}$) visible in the thermal image in the steepest part of the slope (Figure 9).

In the cavity of GZ4, measurements of CO₂ concentration in the air were performed as a function of height from the ground and distance from the cavity wall. At 25 cm height, values were higher than 0.5% up to 5 m from the cavity (Text S2.2 in the supporting information), thus defining a CO₂ pool close to the ground in the recess of the cavity.

4.6. Estimation of Total CO₂ and Radon Degassing

Using the CO₂ and radon flux data collected on the ground in each gas zone, the total degassing (“discharge”) of both gases could be estimated. This estimate was calculated by preparing a map of the available values and then performing kriging and interpolation of the available data set, with the values of each point used in the calculation being averaged from the measured values. A sensitivity analysis was performed to assess the uncertainty on these spatially integrated numbers. This consisted of randomly varying each point within its associated error bar and varying the radius of the interpolation (the main parameter controlling the spatial average of the interpolation algorithm). In total, for two different values of this radius, 10 calculations were performed, one using the flux data and the other nine using the randomly varied flux data. These simulations were averaged, and the standard deviation was assigned as the error bar of the total discharge.

A requirement of both practical and theoretical importance in the measurement of the total discharge is to have some knowledge of the minimum number of points and the possible spatial distributions that determine a given uncertainty and, if possible, to have some idea of the optimal configuration. The spacing of measurement points is of concern, particularly if (small) anomalous areas are present [Viveiros *et al.*, 2010]. In the SBHS, in newly discovered gas zones, it was often the case that time was limited, and, in the case of radon, practical considerations meant that a maximum of 37 scintillation flasks could be carried into the field each day. Consequently, dedicated Monte Carlo simulations, detailed in Appendix A, were performed to study this optimization problem. The optimization study was based on a number of 40 CO₂ flux measurements, with a typical point spacing of 4 m, scattered on a surface of circa 1200 m². Different approaches were tested, and their relative merits are discussed in Appendix A.

Contrary to expectations, the more accurate deployment technique in an unknown potential gas zone was not a simple regular mapping using a small number of profiles, an approach which was used in an earlier investigation of GZ1 [Perrier *et al.*, 2009]. The best technique was an adaptive strategy in which gas flux measurement profiles were performed iteratively, in such a way that the profiles at any iteration always passed through the highest point that had been measured in all preceding profiles, but perpendicular

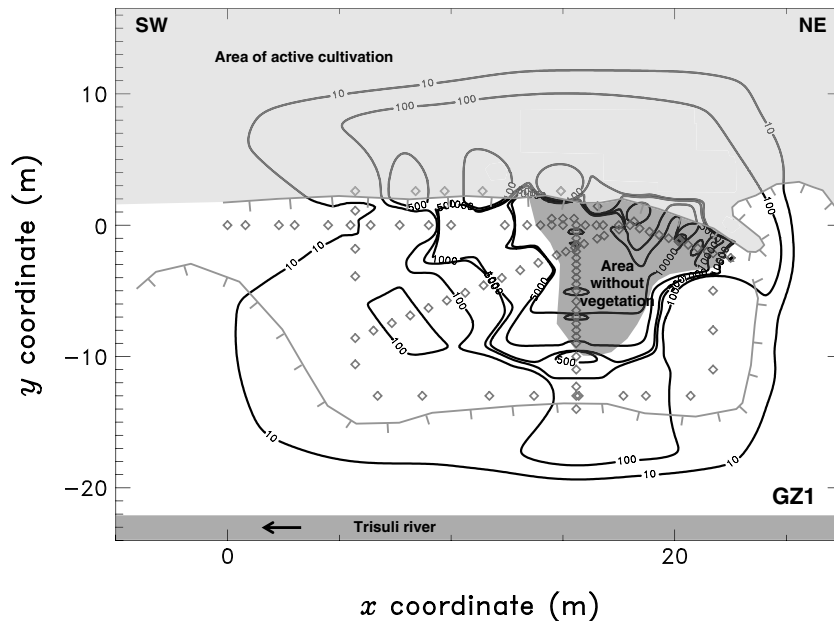


Figure 13. Example of estimation of total CO₂ discharge in GZ1. Data points and contours of the CO₂ fluxes expressed in $\text{g m}^{-2} \text{d}^{-1}$ are shown. This example yields an estimated total CO₂ discharge of $1.37 \pm 0.27 \text{ t d}^{-1}$. Coordinates (0, 0) correspond to 28.16273°N , 85.33745°E .

(or close to perpendicular) to them. When such a strategy was implemented, the simulations indicate that with some justifiable assumptions regarding the spatial structure of the discharge, values of the integrated discharge can be obtained with an uncertainty of circa 20%. This uncertainty was considered sufficient for the current purpose, and because of the difficulty of identifying and measuring many of the points with the highest fluxes, these estimates should be considered with caution and generally as lower estimates.

Examples of results for the estimated total CO₂ discharge are shown in Figure 13 for GZ1 and in Figure 14 for GZ3. In all estimations, the average CO₂ and radon fluxes of background areas were subtracted, thus consistently defining the threshold values which delineate the gas zone areas. In GZ1 (Figure 13), CO₂ flux measurements were performed along profiles that circumscribed the area of high degassing, hence giving a robust average estimation of the total CO₂ discharge of $1.4 \pm 0.3 \text{ t d}^{-1}$. In GZ3 (Figure 14), one vertical profile associated with several horizontal profiles of CO₂ flux yielded sufficiently accurate average estimated value of the total CO₂ discharge of $2.5 \pm 0.5 \text{ t d}^{-1}$. Averages of the estimated total CO₂ and radon discharges obtained with the same method are summarized in Table 2, for each gas zone individually and all gas zones aggregated together. A relatively important CO₂ release from the cavity in GZ4 has been obtained, thus potentially increasing the overall estimate of the total CO₂ degassing of GZ4 (Text S2.2 in the supporting information).

5. Discussion

5.1. Radon Flux as a Proxy for CO₂ Flux

In the SBHS, where both CO₂ and radon fluxes were measured at the same points on the ground, the relationship between the CO₂ and radon fluxes was evaluated by calculating the correlation coefficient, R , between them. The uncertainty was estimated by Monte Carlo simulation as the standard deviation of 30 simulations of the correlation coefficient. The correlation coefficient values are summarized in Table 2 and are highly significant.

For background areas, the correlation is shown in Figure 15. From the whole data set (73 points), a correlation coefficient $R = 0.76 \pm 0.02$ was obtained. Moreover, for the profile GPX (black diamonds in Figure 15), for which there is a significant number (37) of data points, various elongated parallel features appear, showing a

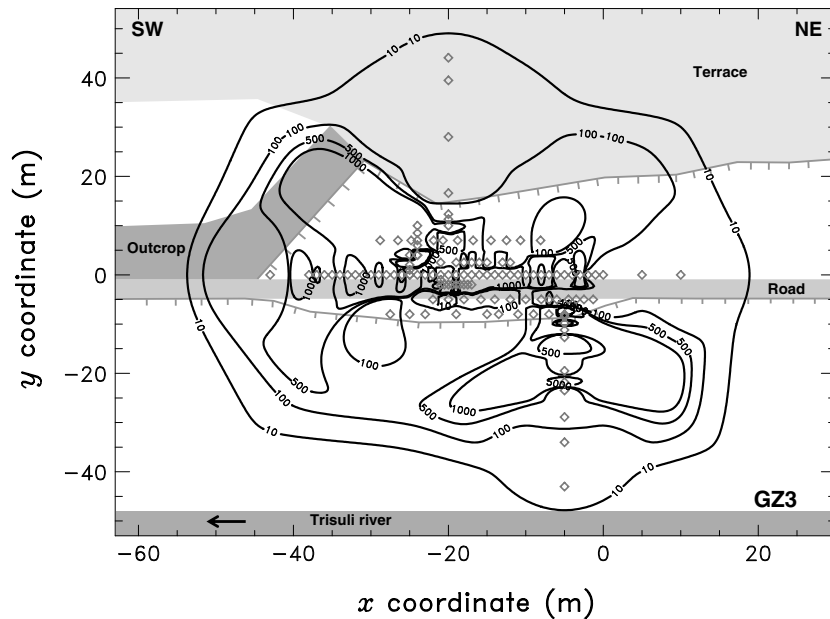


Figure 14. Example of estimation of total CO₂ discharge in GZ3. Data points and contours of the CO₂ fluxes expressed in g m⁻² d⁻¹ are shown. This example yields an estimated total CO₂ discharge of 2.49 ± 0.50 t d⁻¹. Coordinates (0, 0) correspond to 28.15925°N, 85.33513°E.

trend from smaller to higher fluxes. Thus, in GPX, the data suggest the existence of scaling laws with the same slope and shifted normalizations.

For GZ1–GZ5, the relationship between CO₂ flux and radon flux (240 points) is presented in Figure 16, in association with background values of Figure 15 (data are available in Table S1 in the supporting information). The values of CO₂ and radon flux range over 6 and 5 orders of magnitude, respectively. The smallest fluxes obtained in the five gas zones occur at the edge of the gas zones and tend toward background values, suggesting that the gas zones were properly circumscribed, which is important for the estimation of the aggregated discharge. For the aggregated zones, the overall correlation coefficient was $R = 0.86 \pm 0.02$, the highest for GZ2 ($R = 0.96 \pm 0.02$) and GZ3 ($R = 0.94 \pm 0.02$), and the smallest for GZ4 ($R = 0.89 \pm 0.07$). In more detail, GZ1 data show slightly smaller radon flux for given high CO₂ flux than GZ3 data, and GZ3 and GZ4 data appear similar for both small and high CO₂ fluxes (Figure 16). A significant correlation was also

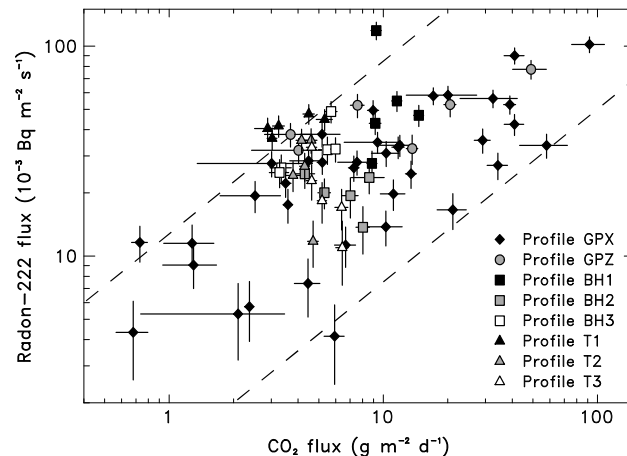


Figure 15. CO₂ flux versus radon flux for the whole background data set. Each point corresponds to one profile located in Figures 1 and 2.

observed between CO₂ fluxes and SP anomalies in GZ1 (Text S3.1 in the supporting information).

This implies a relationship between the two fluxes for a major part of the ranges of magnitudes at least, and to a first approximation, the relationship between the two gas fluxes for the aggregated zones follows a power law (Figure 16): $\Phi_{Rn} = a\Phi_{CO_2}^b$, with $a = 2.2 \pm 0.2$, $b = 0.74 \pm 0.02$, and good coefficient of determination $R^2 = 0.85 \pm 0.03$.

Radon has a diffusion length of up to a few tens of centimeters in rocks and soils and needs a carrier gas to be transported at significant distances from

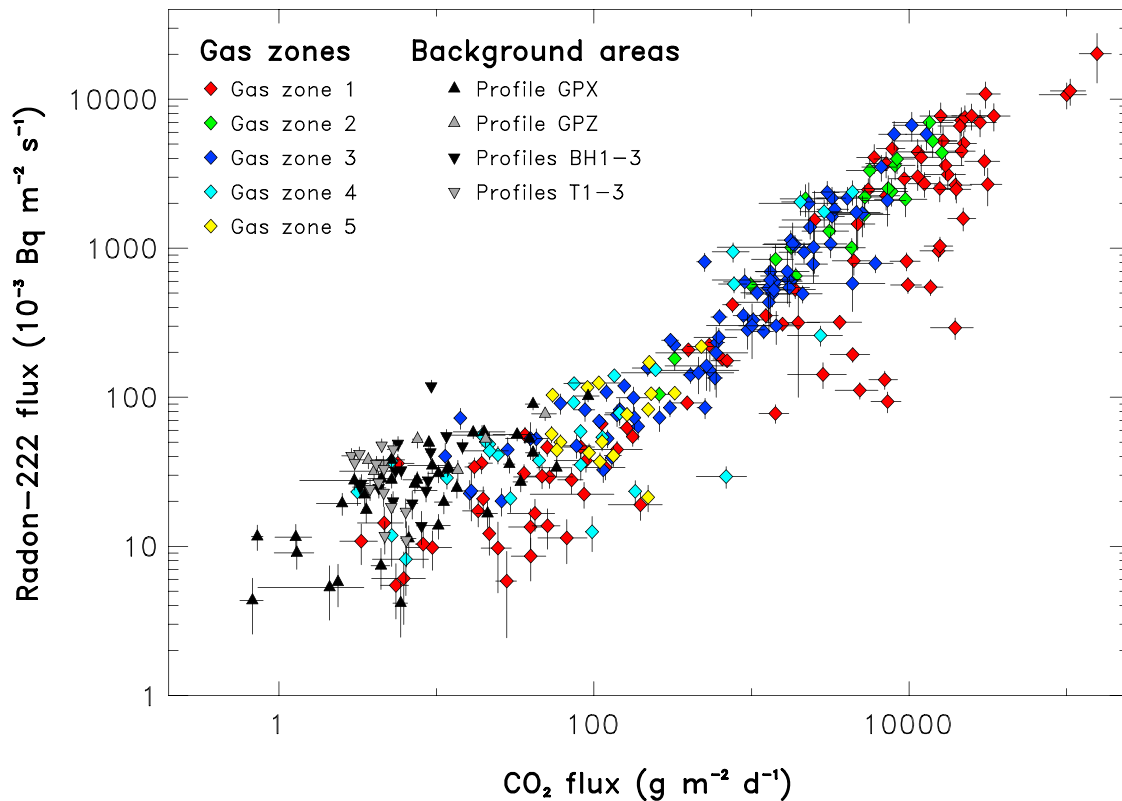


Figure 16. CO₂ flux versus radon flux for the whole gas zones and background data set of the SBHS in the dry winter season. This data set is available in Table S1 in the supporting information.

its source to the atmosphere. Such a carrier gas can be, for example, air, CH₄, H₂, and CO₂ [e.g., *Etiopie and Lombardi*, 1995]. The current results show a high correlation between CO₂ and radon fluxes, indicating that CO₂ is a significant carrier of radon, with a systematic, characterizable power law relationship.

The correlations observed in this study are better than the first correlation drawn by *Perrier et al.* [2009]. Moreover, these more recent correlations are relatively consistent for all gas zones in the dry winter season, confirming an observation demonstrated previously only for GZ3 [*Girault et al.*, 2009]. Therefore, using this correlation and measuring only radon as a CO₂ proxy in the field, noting that radon probes and sensors are more robust, reliable, and cost effective than their CO₂ counterparts for long-term monitoring, information about CO₂ release could be obtained efficiently from radon data.

However, the precise correlation between CO₂ and radon is site dependent, and therefore, both must be studied to establish the relationship before radon flux can be used to make inferences regarding CO₂ flux. To understand this complex but significant relationship, a sufficiently detailed radon-CO₂ transport model is needed, based on a sufficiently exhaustive determination of the radon sources. Such a study is presented in the companion paper [*Girault and Perrier*, 2014].

5.2. Effect of CO₂ Flux on Soil Effective Radium Concentration

The results of effective radium concentration (EC_{Ra}) of soil samples, ranging from 2.4 to 28 Bq kg⁻¹, are within the same range of variation encountered in other areas throughout the world, such as in Europe [*Stoulos et al.*, 2004; *López-Coto et al.*, 2009; *Breitner et al.*, 2010], America [*Ingersoll*, 1983; *Greeman and Rose*, 1996; *Williams-Jones et al.*, 2000], and Asia [*Megumi and Mamuro*, 1974; *Singh et al.*, 2008]. In comparison with available EC_{Ra} data of soils collected in the Kathmandu Valley (Nepal) and in other locations along the Trisuli River [*Girault et al.*, 2011a, 2011b], soils of the SBHS have a smaller average value and a smaller range of variation.

Table 4. Summary of Data From Selected Radon Flux Studies Available in the Literature Obtained in Uranium Mining/Milling Sites, in Volcanic, Hydrothermal and Mofette Sites, and in Fault and Geology-Related Areas and Ordered From Lowest to Highest Mean Radon Flux^a

Reference Name	Country	Site	Measured Radon-222 Flux (10^{-3} Bq m ⁻² s ⁻¹)				Reference
			No. of Measurements	Mean	Min	Max	
U milling/mining sites (10)							
Pridnieprovsky	Ukraine	Chemical Plant, various tailing dumps	1050	42	20	71,000	Lavrova and Voitsekhovych [2013]
Japanese mines	Japan	Various U mines, mill tailing dam	107	71.4	11	3500	Ishimori and Maruo [2005]
Kövágószőlős	Hungary	Kövágószőlős, near tunnel of closed mine	7	623	208	1167	Somlai et al. [2006]
Wood Mine	USA	Central City Wood Mine, Colorado, ²³⁸ U bearing rock outcrops	620	2883	10	7800	Pearson and Jones [1966]
Jaduguda	India	Jaduguda, undisturbed natural soil, tailings piles	>12	5336	16	25,410	Jha et al. [2000, 2001], Sahoo et al. [2010]
Nabarlek	Australia	Nabarlek, Northern Territory, postmining, control sites	8	8356	591	47,040	Bollhöfer et al. [2006], Mudd [2008]
Grants	USA	Grants, New Mexico, ²³⁸ U bearing rock outcrops	6	16,310	14,740	18,570	Pearson and Jones [1966]
Shaoguan	P.R. China	Shaoguan, Guangdong Province, tailings	8	17,572	76	126,502	Tan et al. [2012]
Ranger	Australia	Ranger, Northern Territory, tailings, laterite, ore stockpiles	>87	32,300			Mudd [2008], Lawrence et al. [2009]
Los Ratones	Spain	Los Ratones, three slag heaps					Lozano et al. [2000]
Volcanic, hydrothermal, and mofette sites (6)							
Tantloi	India	Thermal spring Tantloi, Bihar	9	178	500	750	Das et al. [1998]
Cava Selci	Italy	Cava dei Selci, Alban Hills	114	28.3	28.3	1653	Tuccimei and Soligo [2008]
Hsiao-You-Keng	Taiwan	Hsiao-You-Keng hydrothermal area, Tatun Volcano Group	7	199	80	543	Yang et al. [2011]
Niška Banja	Serbia	Niška Banja spa, near houses downtown	6	207	30	1542	Žunić et al. [2006]
Solfatara	Italy	Solfatara of Puzzuoli Volcano, Phlegraean Fields	54	211	0	1074	Voltattorni et al. [2009]
SBHS	Nepal	Syabru-Bensi hydrothermal system	446	259	1.2	38,500	This study
Fault- and geology-related sites (4)							
Kunlun Fault	China	Xidatan segment, Kunlun Fault, Qinghai Province	≈60	14.1		538	Richon et al. [2010]
Trassaco Fault	Italy	Trassaco Fault, Fucino Plain	16	18.3		53.3	Ciotoli et al. [2007]
SBGM Fault	Italy	San Benedetto-Giola dei Marsi Fault, Fucino Plain	16	24.4		119.5	Ciotoli et al. [2007]
Bretagne	France	South of Bretagne, granites-leucogranites	≈100	72.3	9	837	Ielsch et al. [2001]

^aSee Table 5 caption for the definition of the groups.

At sites where measurements of CO₂ flux, radon flux, and EC_{Ra} of soil were performed (mainly GZ1–GZ3), EC_{Ra} was consistently observed to be affected by the fluid release. Indeed, in Figures 6, 8, and 9, the EC_{Ra} data show a relatively convex shape in the large degassing areas, with moderately higher values in the center and notable smaller values at the boundaries. It has been proposed that molecules of CO₂ gas, transported rapidly through soils to the atmosphere, might be able to entrain and disperse the small size soil particles associated with higher radium concentration [Greeman and Rose, 1996; Breiter et al., 2010]. Alternatively, although such effects are poorly known in soils, CO₂ might affect radon adsorption: CO₂ is known to decrease the adsorption potential for radon on activated charcoals and silica gels [Meslin et al., 2011]. Also, the presence of dissolved CO₂ in water might increase radium dissolution and hence transport in solution.

5.3. Total CO₂ and Radon Discharge in the SBHS

Over the period 2007–2011, CO₂ flux, radon flux, radon concentration, SP, and carbon isotopic ratio measurements were found to be relatively consistent (Text S3.2 in the supporting information), suggesting stable pattern of degassing over the SBHS, a point which is discussed further in the companion paper [Girault and Perrier, 2014].

On the basis of all the information (section 4 and Table 2) and noting the findings of Viveiros et al. [2010] in another context, it can be assumed that the CO₂ and radon fluxes obtained in the background areas are mainly of biological and nonhydrothermal origin. Thus, it can be deduced that the “excess” CO₂ fluxes, and corresponding radon fluxes, above background in the five gas zones, GZ1–GZ5, correspond to hydrothermal degassing.

The two zones with the most CO₂ and radon flux measurements are GZ1 and GZ3. GZ1 is characterized by high fluxes over a relatively small ground area (circa 130 m²) whereas GZ3 is characterized by relatively smaller fluxes over a wider area (circa 1350 m²). However, these two gas zones are ultimately defined by broadly similar total CO₂ discharges, 1.4±0.3 t d⁻¹ for GZ1 and 2.5±0.5 t d⁻¹ for GZ3, although the total radon discharge for GZ1, 19 ± 4 MBq d⁻¹, is approximately one fifth of that of GZ3, 90 ± 18 MBq d⁻¹. Gas zones GZ2 and GZ4 have similar total discharges of both CO₂ and radon, whereas GZ5 is the least important radon degassing area of the SBHS.

Aggregating all five gas zones yields total CO₂ and radon discharges of 5.9 ± 1.6 t d⁻¹ and 140 ± 29 MBq d⁻¹, respectively. This value for CO₂ degassing is 6 times that of the first calculation performed by Perrier et al. [2009], which was solely based on GZ1. Although significant, these amounts should be regarded as lower estimates because it can be assumed that there are other similar but

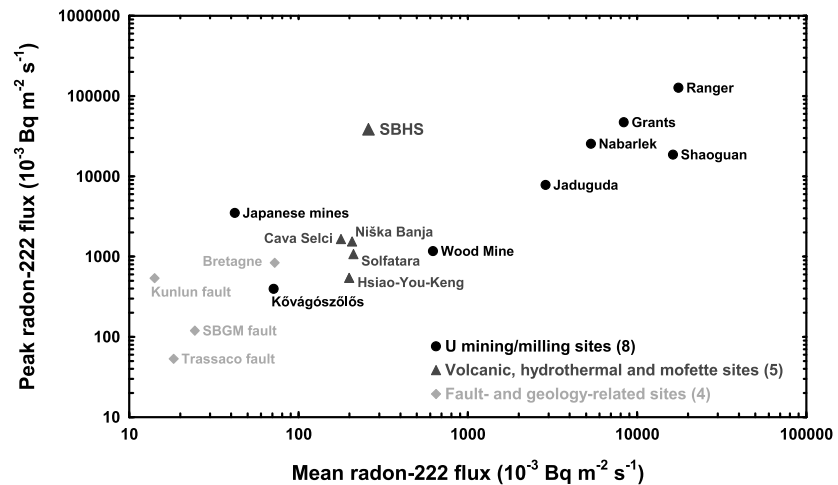


Figure 17. Mean radon flux versus peak radon flux for selected natural sites reported in the literature (see Table 4).

as yet unidentified gas zones in the SBHS, as illustrated by the element of luck in the discovery of GZ4 in this research. In addition, the highest flux values, often occurring along cracks or collapsing terrace scarps, are all but impossible to measure. However, even with such considerations, the overall area of degassing is not insignificant. We define the effective area of strong degassing as the area where CO_2 flux is higher than $500 \text{ g m}^{-2} \text{ d}^{-1}$ and where radon flux is higher than $250 \times 10^{-3} \text{ Bq m}^{-2} \text{ s}^{-1}$. For GZ1–GZ5 combined, we obtain an area of circa 1600 m^2 .

Such an estimation of total radon discharge based on flux measurements on the ground has not previously been attempted in natural systems. However, radon flux has been measured in a number of various locations worldwide. The high geometric mean ($259 \times 10^{-3} \text{ Bq m}^{-2} \text{ s}^{-1}$) and the exceptional peak ($38,500 \times 10^{-3} \text{ Bq m}^{-2} \text{ s}^{-1}$) of radon flux in the SBHS can be compared with other sites (Table 4). To illustrate this, the mean radon flux is shown versus the peak radon flux for selected sites (Figure 17). The mean radon flux of the SBHS appears similar to the mean values observed in other natural sites, such as volcanic [Voltattorni *et al.*, 2009], hydrothermal [Yang *et al.*, 2011], and mofette sites [Žunić *et al.*, 2006; Tuccimei and Soligo, 2008]. The peak radon flux of the SBHS is 1 and 2 orders of magnitude higher than the peaks measured in those same volcanic, hydrothermal, and mofette sites and in fault- and geology-related sites [Ielsch *et al.*, 2001; Ciotoli *et al.*, 2007; Richon *et al.*, 2010], respectively, but appears compatible with peaks obtained in some American, Australian, and Chinese uranium mining sites [Pearson and Jones, 1966; Bollhöfer *et al.*, 2006; Mudd, 2008; Tan *et al.*, 2012]. As a result, the peak radon flux highlights the uniqueness of the SBHS, compared with other natural sites (Figure 17).

The estimated total CO_2 discharge of the SBHS (circa 5.9 t d^{-1}) can be compared with other CO_2 discharges assessed using ground surface CO_2 flux measurements at various sites throughout the world (Table 5). The SBHS value appears smaller than most CO_2 discharges of volcanic, geothermal, and hydrothermal sites. Nevertheless, the SBHS value is similar to some volcanic sites, such as La Fossa (Italy) [Carapezza *et al.*, 2009] and White Island (New Zealand) [Wardell *et al.*, 2001]; some geothermal sites, such as Dixie Valley (USA) [Bergfeld *et al.*, 2001] and Mazarón-Gañuelas Tertiary Basin (Spain) [Rodrigo-Naharro *et al.*, 2013]; and some hydrothermal sites, such as Long Valley (USA) [Bergfeld *et al.*, 2006]. In general, the CO_2 discharge of the SBHS is compatible with the majority of mofette sites, such as Selvena (Italy) [Rogie *et al.*, 2000], Stavešinci (Slovenia) [Vodnik *et al.*, 2009], and Hartoušov (Czech Republic) [Kämpf *et al.*, 2013], but appears orders of magnitude higher than estimated values of fault-related sites, such as Peloritani Monts (Italy) [Giammanco *et al.*, 2008], San Andreas and Calaveras faults (USA) [Lewicki *et al.*, 2003a], and Kunlun fault (China) [Richon *et al.*, 2010].

One interesting point of comparison remains the surface area of high CO_2 degassing, circa 1600 m^2 in the SBHS. This is one of the smallest areas investigated to date (2013) which yields such a large CO_2 discharge and an exceptional peak CO_2 flux ($236,000 \text{ g m}^{-2} \text{ d}^{-1}$). For example, the SBHS releases 5 times more CO_2 gas over the same surface area than Vesuvio cone (Italy) [Granieri *et al.*, 2010]. Furthermore, the peak value appears to

Table 5. Summary of Data From Selected CO₂ Flux Studies Available in the Literature Obtained in Volcanic (Holocene Active Volcanoes), Geothermal (Economically Viable Energy Currently Produced), Hydrothermal (Water Boiling Temperature Reported at the Surface), Mofette (Colder Gas Temperature, Typically <50°C), and Fault-Related Sites (a Faulted Region) and Ordered From Lowest to Highest Total CO₂ Degassing

Reference Name	Country	Site	Measured CO ₂ Flux (g m ⁻² d ⁻¹)					Estimated Total CO ₂ Degassing (td ⁻¹)	Estimated Surface of CO ₂ Degassing (km ²)	Reference
			No. of Measurements							
			Min	Mean	Max	Min	Max			
Volcanic sites (42)										
N. Cannestra	Italy	Nel Cannestra, Stromboli Island	226	115	1	1244	0.4	0.0047	Carapezza et al. [2009]	
Vesuvio	Italy	Vesuvio cone	1815	515	116	2100	1.18	0.0015	Granieri et al. [2010]	
Tor Cald.	Italy	Tor Caldara, Alban Hills	61	134 ^a	1000	1000	1.53	0.0114	Carapezza et al. [2012]	
Methana	Greece	Methana volcanic system, NE Peloponnesus	39	236	0.1	894	2.42	0.0101	D'Alessandro et al. [2008]	
La Fossa	Italy	Pizzo Sopra La Fossa, Stromboli Island	838	1614	1	47,970	8.3	0.0069	Carapezza et al. [2009]	
White Isl.	N. Zealand	Near crater, White Island	19	44	2	4370	8.7	0.2	Wardell et al. [2001]	
Cava Selci	Italy	Cava dei Selci, Alban Hills	159	1522 ^a	4000	4000	12.5	0.0082	Carapezza et al. [2012]	
S-Shinzan	Japan	Showa-Shinzan, Hokkaido	157	16	0.03	552	14.8	0.53	Hernández et al. [2006]	
NK Isl.	Greece	Nea Kameni Islet, Santorini	63	552 ^a	1.6	6565	15.4	0.028	Chiodini et al. [1998]	
Masaya	Nicaragua	Masaya Volcano	707	2750	1	50,000	19	0.0103	Lewicki et al. [2003b]	
R. Grande	Italy	Rina Grande, Stromboli Island	340	1084	1	22,288	26.9	0.0363	Carapezza et al. [2009]	
Etna SML	Italy	Santa Maria di Licodia, Etna, Sicily	524	15.4	0.2	166	27.5	2.5	Giammanco et al. [2010]	
Ukinrek	USA	Ukinrek Maars, Alaska	131	919 ^a	0	11,700	32.5	0.04	Evans et al. [2009]	
Epomeo	Italy	Mont Epomeo, Donna Rachele, Ischia Island	336	43	0.1	4000	32.6	0.8625	Chiodini et al. [2004]	
NK sum.	Greece	Nea Kameni summit, Santorini	71	394	0.1	25,281	38	0.0196	Parks et al. [2013]	
Usu	Japan	Usu Volcano, Hokkaido	630	15	0.1	9090	39	2.65	Hernández et al. [2001b]	
AVF	N. Zealand	Auckland Volcanic Field	1094	27.1	0	203	61.8	83.8	Mazot et al. [2013]	
Solfatara c.	Italy	Solfatara of Pozzuoli crater, Phlegraean Fields	144	946	30	21,950	79	0.05	Tassi et al. [2013]	
Satsuma	Japan	Satsuma-Iwojima Volcano	155	32	0.01	5640	80	2.5	Shimoike et al. [2002]	
Nisyros	Greece	Caldera, Nisyros Island	2883	39.7 ^a	0.01	6175	84	2	Cardellini et al. [2003b]	
S. Pomezia	Italy	Solfiorata di Pomezia, Alban Hills	356	389 ^a	1500	1500	89.2	0.229	Carapezza et al. [2012]	
Vulcano	Italy	Vulcano crater, Vulcano Island	244	206	0	1416	91	0.2382	Inguaggiato et al. [2012]	
Cuicocha	Ecuador	Lake-filled, Cuicocha Volcano	172	8	48.5	48.5	106	13.3	Padrón et al. [2008]	
M.-jima	Japan	Miyake-jima Volcano, Izu Islands	265	190	0.1	18,150	120	0.66	Hernández et al. [2001a]	
Hakkoda	Japan	Hakkoda Volcano, Honshu	180	1110 ^a	14	38,142	127	0.58	Hernández et al. [2003]	
V. Cupella	Italy	Valle di Cupella, Alban Hills	37	3325	4	54,000	133	0.04	Carapezza and Turchini [2007]	
El Ch.	Mexico	Crater lake and floor, El Chichón Volcano	418	1102	156	14,031	144	0.13	Mazot et al. [2011]	
Etna WR	Italy	Western flank Rift, Etna, Sicily	1616	13.8	0.2	312	166	14	Giammanco et al. [2010]	
Timanfaya	Spain	Timanfaya Volcanic Field, Lanzarote, Canary Islands	3128	0.91	0	34	181	252	Hernández et al. [2012a]	
Merapi	Indonesia	Merapi Volcano cone	220	364	0	3300	215	0.632	Toutain et al. [2009]	
Etna mud	Italy	Mofettes and mud volcanoes, Etna, Sicily	712	33	0	5726	225.5	0.1465	Giammanco et al. [2007]	
Pululahu	Ecuador	Caldera, Pululahu Volcano	217	10	141.7	141.7	270	27.6	Padrón et al. [2008]	
Teide	Spain	Teide caldera, Tenerife, Canary Islands	100	2382	393	4477	380	0.53	Hernández et al. [1998]	
Iwojima	Japan	Iwojima Volcano	424	6.7	0	7450	450	22	Notsu et al. [2005]	
Hengill	Iceland	Hengill volcanic system	752	9.1	0	17,666	453	168	Hernández et al. [2012b]	
S. Negra	Ecuador	Caldera, Sierra Negra Volcano, Galapagos archipelago	331	14.3	0.5	22,368	605	69.4	Padrón et al. [2012]	

Table 5. (continued)

Reference Name	Country	Site	Measured CO ₂ Flux (g m ⁻² d ⁻¹)				Estimated Total CO ₂ Degassing (t d ⁻¹)	Estimated Surface of CO ₂ Degassing (km ²)	Reference
			No. of Measurements	Mean	Min	Max			
Pantelleria	Italy	All Pantelleria Island	146	10.4	1.6	1260	953	84	Favara et al. [2001]
Furnas	Portugal	Furnas, São Miguel Island, Azores	2605	404	0	25,000	968	4.8	Viveiros et al. [2010]
Ischia	Italy	All Ischia Island	106	36.3	0	1082	1279	46	Pecoraino et al. [2005]
Ustica	Italy	All Ustica Island	28	153	19	666	1323	8.65	Etope et al. [1999]
Solfatara	Italy	Solfatara di Pozzuoli, Phlegraean Fields	414	1300 ^a	3	30,987	1513	1.4	Cardellini et al. [2003b]
Cerro Negro	Nicaragua	Cerro Negro Volcano	300	429	0.5	35,000	2800	0.58	Salazar et al. [2001]
Geothermal sites (8)									
Salton Sea	USA	Salton Sea geothermal system, California	81	143	1	3700	7.31	0.051	Mazzini et al. [2011]
Dixie Valley	USA	Dixie Valley, Nevada	154	53	0.3	570	7.5	0.14	Bergfeld et al. [2001]
M.-G. Basin	Spain	Mazarrón-Gañuelas Tertiary Basin	1036	20	0.3	330	8.9	0.5241	Rodrigo-Naharro et al. [2013]
Reykjanes	Iceland	Reykjanes geothermal area	352	56 ^a	0.3	159	13.5	0.22	Fridriksson et al. [2006]
Sousaki	Greece	Sousaki geothermal system	101	3630	1	33,500	54.4	0.015	D'Alessandro et al. [2006]
Yangbajain	China	Yangbajain geothermal field, Tibet	331	43 ^a	1	7000	138	3.2	Chioldini et al. [1998]
Latera	Italy	Latera Caldera	1089	278	2.8	53,000	350	3.1	Chioldini et al. [2007]
Rotorua	N. Zealand	Ngapuna/Sulphur Bay, Rotorua	956	204		11,535	620	8.9	Werner and Cardellini [2006]
Hydrothermal sites (11)									
HYK	Taiwan	Hsiao-You-Keng hydrothermal area, Tatun Volcano	8	189	12	11,482	2.17	0.0115	Yang et al. [2011]
Long Valley	USA	Long Valley caldera, California	730	118	0.4	1810	8.7	0.0466	Bergfeld et al. [2006]
LHK	Taiwan	Liu-Huang-Ku hydrothermal area, Tatun Volcano	257	621 ^a	16	8079	21.1	0.034	Lan et al. [2007]
S. secca	Italy	Solfatara secca, Poggio dell'Olivo, Viterbo	96	2396	14	22,048	23	0.0096	Cardellini et al. [2003a]
Soda Spr.	USA	Soda Springs, Idaho	178	980	1	52,178	49	0.05	Lewicki et al. [2013]
Yellowstone HSB	USA	Hot Spring Basin, Yellowstone, Wyoming	228	320	2	14,000	63.5	0.155	Werner et al. [2008]
Horseshoe	USA	Horseshoe Lake, Mammoth Mountain, California	313	800 ^a	5.7	8670	104.3	0.13	Cardellini et al. [2003b]
Ohaaki	N. Zealand	Ohaaki field, Taupo Volcanic Zone	2663	144	3	32,000	111	12.7	Rissmann et al. [2012]
Manziana	Italy	Caldara di Manziana, Viterbo	200	1600		10,000	200	0.104	Chioldini et al. [1999]
Poggio	Italy	Poggio dell'Olivo, Viterbo	196	489 ^a	0.5	8797	234	0.82	Cardellini et al. [2003b]
Yellowstone MV	USA	Mud volcanoes, Yellowstone, Wyoming	410	1712 ^a	4	32,600	390	3.45	Werner et al. [2000]
Mofettes sites (4)									
Hartoušov	Czech Republic	Hartoušov and Bubiák, Eger Rift	762	5327 ^a	15	59,465	2.18	0.075	Kämpf et al. [2013]
Stavešinci	Slovenia	Stavešinci field	66	877	259	1020	2.63	0.003	Vodnik et al. [2009]
SBHS	Nepal	Syabru-Bensi hydrothermal system	1108	418	2	236,000	5.93	0.0016	This study
Selvena	Italy	Selvena	90	820			9	0.011	Rogge et al. [2000]
Fault-related sites (5)									
Kunlun	China	Xidatan segment, Kunlun Fault, Qinghai Province	60	12.9		421	0.06	0.0045	Richon et al. [2010]

Table 5. (continued)

Reference Name	Country	Site	Measured CO ₂ Flux (g m ⁻² d ⁻¹)				Estimated Total CO ₂ Degassing (td ⁻¹)	Estimated Surface of CO ₂ Degassing (km ²)	Reference
			No. of Measurements	Mean	Min	Max			
San Andreas	USA	San Andreas Fault, near Parkfield, California	646	19	4	107	0.23	0.012	Lewicki et al. [2003a]
Peloritani Mts	Italy	Peloritani Monts, Sicily	26	24.6	4.3	58.8	0.29	0.0077	Giannanco et al. [2008]
Calaveras	USA	Calaveras Fault, near Hollister, California	436	55	10	428	0.71	0.013	Lewicki et al. [2003a]
Tuscany	Italy	Faulted grassland, Tuscany	10	81	32	194	14.58	0.18	Etioppe [1999]

^aArithmetic mean.

be the highest CO₂ flux ever measured, even above the 128,600 g m⁻² d⁻¹ reported in the Solfatara of Pozzuoli (Italy) [Werner et al., 2003] and the anomalous 90,000 g m⁻² d⁻¹ of the automatic station at La Fossa, Stromboli (Italy) [Rizzo et al., 2009] and much larger than the circa 50,000 g m⁻² d⁻¹ reported in several volcanic and geothermal sites, such as Valle di Cupella (Italy) [Carapezza and Tarchini, 2007], Masaya (Nicaragua) [Lewicki et al., 2003b], Latera caldera (Italy) [Chiodini et al., 2007], and in the recent study of Hartoušov mofette field [Kämpf et al., 2013].

The compiled data of estimated total CO₂ degassing (Table 5) are shown as a function of peak CO₂ flux (Figure 18a) and of the estimated surface area of high CO₂ degassing (Figure 18b). In Figure 18a, approximately two thirds of the volcanic, geothermal, and hydrothermal sites are characterized by peak CO₂ flux values between 3000 and 60,000 g m⁻² d⁻¹ and total CO₂ degassing ranging from 7 to 1000 t d⁻¹. Some sites are located outside these ranges, such as exceptional degassing sites (Solfatara and Cerro Negro), sites with large surface of degassing (Ischia Island, Ustica Island, Pantelleria Island, Cuicocha, Pululahua, and Timanfaya), fault-related sites (Peloritani Mountains and San Andreas and Calaveras faults), and mofette sites (Stavešinci, Hartoušov, and SBHS). In Figure 18b, the total CO₂ degassing shows a remarkable relationship with the surface area of high CO₂ degassing. While volcanic, geothermal, and hydrothermal sites range from low (0.4 t d⁻¹) to high (2800 t d⁻¹) total CO₂ degassing over extremely small (0.0015 km²) to extremely large (252 km²) surfaces, mofette and fault-related sites are characterized by intermediate (<10 t d⁻¹) and low (<0.8 t d⁻¹) total CO₂ degassing, respectively, both over relatively small surfaces (<0.1 km²). Furthermore, the relationship between total CO₂ degassing (*D*) and surface area (*S*) follows a power law (Figure 18b), *D* = *aS^b*, with significantly different parameter values for volcanic sites (*a* = 94 and *b* = 0.44) and the other sites aggregated together (*a* = 85, *b* = 0.71).

Using the power law obtained for volcanic sites, we can attempt to extrapolate the total CO₂ degassing on the ground of all volcanoes throughout the world, knowing their total estimated surface. In a first approximation, we can take into account the subaerial Holocene active volcanoes, referenced in the Worldwide Holocene Volcano database of the Smithsonian Institution, Washington (<http://www.volcano.si.edu/world/>; Siebert and Simkin, 2002). We approximate the shape of all volcanoes (whatever the type) with a cone. Using summit altitude, average altitude at the base of the cone and assuming a consistent angle with horizon at the summit of the cone (aperture and opening angle), we obtain an estimated total surface area of subaerial Holocene active volcanoes of 760,000 ± 100,000 km². Therefore, we calculate an estimated total CO₂ degassing from the flanks of subaerial Holocene active volcanoes of 14 ± 6 Mt yr⁻¹. This value is higher than the reported measured diffuse emissions of subaerial Holocene active volcanoes (6.4 Mt yr⁻¹), but appears more likely than the maximum estimates of 117 Mt yr⁻¹ calculated using the ratio number of studied sites/total number of subaerial volcanoes [Burton et al., 2013]. Our calculation indicates that the global CO₂ degassing of subaerial volcanoes, with currently accepted mean (range, min–max) of 91 ± 17 (20–130) Mt yr⁻¹, is significantly underestimated [e.g., Gerlach, 2011], as recently suggested [Burton et al., 2013]. It is reasonable to add the recent estimate of CO₂ degassing of volcanic lakes (94 ± 17 Mt yr⁻¹) [Pérez et al., 2011] to the values obtained during eruptive and quiescent periods, thus leading to a total estimated CO₂ degassing of subaerial active Holocene volcanoes of 199 ± 40 Mt yr⁻¹, comprising 91 ± 17 (eruptive periods) + 14 ± 6 (diffusive during quiescent periods) + 94 ± 17 (volcanic lakes). This preliminary estimate, compared with currently measured CO₂ flux of subaerial active Holocene volcanoes of circa 73 Mt yr⁻¹ [Burton et al., 2013], suggests that it could be of interest to carry out a more detailed calculation. In addition, CO₂ degassing of fault-related sites is not negligible (Figure 18b), in particular in orogenic belts, but needs more measurements to be extrapolated further.

5.4. Thermal Energy Release

Having estimated a lower bound for the total CO₂ flux (5.9 t d⁻¹) and considering the thermal source from gaseous CO₂ release only, it was possible to assess the corresponding total energy release. Again, this should be regarded as a lower bound as it does not account for contributions from other thermal sources, such as the hydrothermal power dissipation of hot springs at the surface [Derry et al., 2009]. The contributions from such sources are however small in comparison due to the low flow rates of the hot springs for the whole system (maximum 1 L s⁻¹). Thus, in the SBHS as in most volcanic and geothermal sites [Chiodini et al., 2001, 2005; Werner et al., 2008], it can be postulated that most of the thermal energy is

the range of variation of our measured heat fluxes in GZ1, $3.2\text{--}38\text{ W m}^{-2}$ (Figure 6). Similar heat flux values were obtained at Pantelleria Island Volcano (Italy) over a 36 times larger surface area [Chiodini *et al.*, 2005]. Therefore, the gas zones of the SBHS produce relatively significant heat output from a small spatial extent. The SBHS thus appears relevant for the study of heat transport in the particular tectonic context of continental collision away from magmatic activity.

5.5. Helium and Carbon Isotopic Ratios to Constrain the CO₂ Source in the SBHS

5.5.1. Helium Isotopic Ratios in the SBHS

The helium (He) concentrations measured in GZ1 (Table 3) are 10 times higher than those in the air, indicating that the He source is not close to the surface. Moreover, the ratio R/R_A , which is close to zero, indicates a strong excess of radiogenic ⁴He (mainly from uranium and thorium) compared with mantle-derived ³He. Thus, the gas sampled in GZ1 has a typical crustal radiogenic signature, and therefore, any significant mantle contribution of CO₂ can be ruled out in GZ1. This conclusion is likely to be valid also for GZ3 and GZ4, but this could not be verified experimentally during this study.

In Nepal, few values (8) of He isotopic ratios are reported. From the free gas of hot spring waters of the SBHS, R/R_A ratios were low (0.027–0.055) [Becker, 2005] and compatible with our values. In the Marsyandi Valley (midwestern Nepal), R/R_A ratios from free gas and water of hot springs yielded ranges of variation of 0.04–0.14 and 0.018–0.055, respectively [Marty *et al.*, 1996; Becker, 2005]. These data of the MCT zone indicate a crustal source for the gas with no (or little) mantle contribution. This crustal source of He can be compared with the gas characteristics in Tibet where a larger number of data (>50) is available [e.g., Klempere *et al.*, 2013]. In the springs of Tingri Graben (120 km NW from SBHS) and at Daggai Co (65 km NNE from SBHS) in South Tibet, R/R_A ratios were 0.018–0.063 [Newell *et al.*, 2008] and 0.020 ± 0.005 [Hoke *et al.*, 2000], respectively, thus again suggesting a crustal contribution. By contrast, R/R_A ratios obtained further north in Yangbajain Graben (0.11–0.13) [Yokoyama *et al.*, 1999; Hoke *et al.*, 2000] and in other northward sites (0.24–0.38) [Yokoyama *et al.*, 1999], as well as in NW Himalayas in Mount Kailash area (0.27–0.38) [Hoke *et al.*, 2000] and near the Karakorum Fault (0.66) [Klempere *et al.*, 2013] clearly showed mantle contribution. Finally, in the SBHS, CO₂/³He ratio was $>1.74 \times 10^{11}$, consistently higher than mid-ocean ridge basalt domain (2×10^9). This value was similar to CO₂/³He values of Yangbajain Graben and Dzaka Chu Valley in Tibet [Yokoyama *et al.*, 1999; Newell *et al.*, 2008].

5.5.2. Carbon Isotopic Ratios in the SBHS

Carbon isotopic ratios obtained from soil-gas CO₂ (Table 3) show only a small variation over the SBHS. In particular, for GZ1 the values are the same (within 5%) as the three previous values reported by Perrier *et al.* [2009], which indicates a good degree of stability over a 5 year period. Such a consistency of $\delta^{13}\text{C}$ through time is particularly interesting and constitutes a real asset for possible long-term monitoring of geochemical characteristics from both degassing areas and springs.

Although the main hot springs of the SBHS showed no bubbling [Perrier *et al.*, 2009], two secondary springs, SBE1 and TT1, located at a distance of 300 m on the opposite bank of GZ1 and at 1.5 km north from the hydrothermal system, respectively, released gas bubbles. SBE1 had a mean temperature of 51°C, pH of 6.9, $\delta^{13}\text{C}_{\text{DIC}}$ (dissolved inorganic carbon) of 0.5‰ [Perrier *et al.*, 2009], and $\delta^{13}\text{C}_{\text{bubbles}}$ of $-3.6 \pm 0.1\text{‰}$. TT1 had a mean temperature of 24°C, pH of 5.7, $\delta^{13}\text{C}_{\text{DIC}}$ of 12.3‰ [Becker, 2005; Evans *et al.*, 2008], and $\delta^{13}\text{C}_{\text{bubbles}}$ of $-2.2 \pm 0.1\text{‰}$. A similar $\delta^{13}\text{C}_{\text{bubbles}}$ value of -1.98‰ was previously reported for a TT1 sample in 2003 [Becker, 2005].

Thus, it is observed that $\delta^{13}\text{C}_{\text{bubbles}}$ values (-3.6 to -2.2‰) are systematically slightly smaller than $\delta^{13}\text{C}_{\text{GZ}}$ (soil-gas) values in the gas zones (-1.7 to -0.5‰) and much smaller than for $\delta^{13}\text{C}_{\text{DIC}}$ values (0.5 to 12.3‰). This suggests that the bubble CO₂ is not at isotopic equilibrium with the dissolved inorganic carbon. Rather, the bubbles seem to be intermediate between a source gas, which could be characterized by $\delta^{13}\text{C}_{\text{GZ}}$, and the dissolved gas.

5.5.3. Discussion of Isotopic Ratios and the CO₂ Source

These observations can be compared with other $\delta^{13}\text{C}$ values obtained at other sites. In Nepal, few $\delta^{13}\text{C}$ values from the free gas of springs (5) are reported in the MCT zone and varied from -4.2 to -2.0‰ [Becker, 2005; Becker *et al.*, 2008; Evans *et al.*, 2008], which are similar to our measured values. Northward in South Tibet, $\delta^{13}\text{C}$ values from the free gas of springs were smaller in Yangbajain Graben (-9.1 to -6.3‰) [Yokoyama *et al.*,

1999] and reasonably similar (but with larger variations) in the Tingri Graben (-13.1 to -0.3‰) [Yokoyama *et al.*, 1999; Newell *et al.*, 2008]. This suggests that the CO_2 source might be different in South Tibet and that the bubble CO_2 might equilibrate with the dissolved inorganic carbon, in contrast to the SBHS.

The SBHS values appear also to be similar to $\delta^{13}\text{C}$ values from the free gas of the mofette sites in the Vogtland/NW Bohemian region (Germany and Czech Republic). Indeed, in the free gas of the Bad Brambach springs in Germany and of the Plesná, U Mostku, and Kopanina springs in Czech Republic, $\delta^{13}\text{C}$ values were circa -4.5‰ [Weise *et al.*, 2001; Bräuer *et al.*, 2003, 2007, 2011] and from -3.0 to -0.8‰ [Bräuer *et al.*, 2008, 2011], respectively. Directly from the gas of mofettes (Bublák, Dolní Částkov, Hartoušov, and Soos), $\delta^{13}\text{C}$ values ranged from -3.0 to -1.6‰ [e.g., Bräuer *et al.*, 2003, 2008, 2011; Kämpf *et al.*, 2013]. However, by contrast with the SBHS, all R/R_A values were high and varied from 1.4 to 5.9 [Weise *et al.*, 2001; Bräuer *et al.*, 2003, 2007, 2008, 2011; Kämpf *et al.*, 2013]. Thus, in the Vogtland/NW Bohemian region, the isotope signature indicates coupled contributions of metamorphic decarbonation of limestone and mantle-derived CO_2 [Bräuer *et al.*, 2009; Kämpf *et al.*, 2013].

In the SBHS, the carbon isotopic signature $\delta^{13}\text{C}_{\text{GZ}}$ appears compatible with a CO_2 source generated by decarbonation of carbonated sedimentary rocks. This interpretation is also consistent with the constraints derived from He isotope analyses. Such a metamorphic reaction occurs typically at 10–20 km depth [e.g., Aque, 2000]. This decarbonation process of calcite minerals enriches the ^{13}C content in the resulting CO_2 -rich fluid, leading to a 2–4‰ increase of the $\delta^{13}\text{C}$ value of CO_2 under temperature and pressure conditions ranging over 300–800°C and 1–10 kbar (at 4–40 km depth), respectively, compared with the carbon isotope ratio of calcite [e.g., Chacko *et al.*, 1991]. Considering the range of $\delta^{13}\text{C}$ values from Lesser Himalayan carbonates at depth, typically -3.5 to -1.1‰ [Evans *et al.*, 2008], we obtain a $\delta^{13}\text{C}$ value of metamorphic CO_2 between -1.5 and $+2.9\text{‰}$. Our range of $\delta^{13}\text{C}_{\text{GZ}}$ values (-1.7 to -0.5‰) appears compatible with those first-order calculations, suggesting that the CO_2 -rich fluid is subject to only little fractionation between its metamorphic source at depth to the mofettes observed at the surface.

In addition, the narrow range of $\delta^{13}\text{C}_{\text{GZ}}$ values, the small differences between $\delta^{13}\text{C}_{\text{GZ}}$ and $\delta^{13}\text{C}_{\text{bubbles}}$ values, and the temporal stability of the degassing system indicate minor or negligible carbon isotope fractionation due to CO_2 dissolution and degassing from water. Indeed, degassing processes strongly fractionate the carbon isotopes [e.g., Mook *et al.*, 1974] and were proposed by Becker *et al.* [2008] and Evans *et al.* [2008] to explain the range of $\delta^{13}\text{C}_{\text{DIC}}$ values obtained throughout the Nepal Himalayas. By contrast, dissolution and degassing affect the $\delta^{13}\text{C}$ in the gas phase to a lesser extent. Our results thus are compatible with the view that the gas zones represent a degassed deeper aqueous phase, whose remnants in the hydrothermal waters are giving the increased observed values of $\delta^{13}\text{C}_{\text{DIC}}$. Also, these results are not incompatible with the alternative view that the observed gas zones, and in particular in GZ3, represent the original deep metamorphic gas, which can reach the atmosphere through gas-dominated pathways, with little interactions with near-surface groundwater. Such gas transport might be, for example, by dry fault/fracture networks reaching the surface, which are possible in the MCT shear zone, and thus possibly largely independent from hydrothermal circulations. These considerations are explored further in the companion paper [Girault and Perrier, 2014].

6. Conclusion

In this paper, the spatial distribution of the degassing areas in the SBHS has been characterized. At the five identified gas zones, more than 1600 CO_2 flux and 850 radon flux measurements were made, complemented by 100 self-potential and 108 soil effective radium concentration (EC_{Ra}) measurements. From these data, the total CO_2 and radon discharges of the SBHS were estimated and the relationship between CO_2 and radon fluxes established. Clear differences in soil radon concentration between GZ1–GZ2 and GZ3–GZ4 were also observed. Based on its location and on its description, GZ5 could be seen as a possible satellite zone of GZ1 and GZ2. Finally, the values of the isotopic ratios obtained confirmed the previous geochemical models [Becker *et al.*, 2008; Evans *et al.*, 2008], proposing the presence of extensive degassing of metamorphic CO_2 in the Himalayas. The dipolar SP anomaly reported previously [Byrdina *et al.*, 2009] is confirmed by this experiment, adding confidence to the concept that SP is a meaningful parameter of geological fluid discharge [Revil *et al.*, 2012]. The SBHS should therefore also be considered

as a promising natural laboratory to explore temporal anomalies of SP [Perrier *et al.*, 1998, 1999; Legaz *et al.*, 2009].

The gas zones of the SBHS provide a unique natural laboratory where measurement methodologies can be tested in a quantitative and detailed manner. The gas zones also illustrate the diversity of the possible signatures and contexts of degassing which, in turn, indicate that various degassing mechanisms are present at this site. While high fluxes are closely associated with the main hot springs (GZ1 and GZ2), major degassing is also observed away from any hydrothermal activity (GZ3 and GZ4), suggesting that CO₂ might be only marginally interacting with water and, therefore, that extrapolations based solely on parameters extracted from water geochemistry might be unrepresentative.

If the degassing is not controlled by hydrothermal circulations, and instead only partially influenced by these, then finding possible gas zones and estimating the total discharges will be more complicated than previously anticipated. Indeed, in the SBHS, a major proportion of metamorphic CO₂ must percolate independently of hydrothermal circulations and emerge away from hot springs. Thus, the presence of hot springs would appear to be an insufficient basis on which to search for degassing and, hence, a large proportion of the CO₂ produced by the Himalayas might still be undetected. This is especially true if degassing proceeds through areas with moderate flux values, such as in GZ5.

The very existence of such extended zones, where there are no “obvious” clues such as the presence of hot springs or (thermally imaged) warm spots, has major consequences. Also, meaningful estimation of the CO₂ discharge of the Himalayas, even on the scale of the Trisuli watershed, for example, appears as a tremendous challenge that can be addressed only with airborne surveys of CO₂ degassing [e.g., Bateson *et al.*, 2008; Bellante *et al.*, 2013] (with a detection limit of 0.1 to 1 t d⁻¹ over 1000 m² in flat and homogeneous areas) or, more likely, with totally new techniques. The SBHS then could be a major site to evaluate such new techniques.

In order to be able to further evaluate hydrothermal (water-dominated) and nonhydrothermal (gas-dominated) degassing and to support the various hypotheses concerning CO₂ sources and gas transport mechanisms, more information is needed on the various accessible gas zones in the vicinity of hot springs, in other sites of the upper Trisuli Valley and at other hot spring sites along the MCT. So far, the SBHS remains the only known natural system in the world with such high CO₂ and radon fluxes, located in a tectonically active zone away from any magmatic activity. However, before long-term monitoring could be considered, which is only worthwhile provided that it can be maintained over decades, or at least a significant fraction of the cycle of large earthquakes, the Himalayas should be surveyed for other candidate hydrothermal areas.

The large amount of data collected in the SBHS, while largely insufficient to provide a final answer on the CO₂ degassing rate of the whole Himalayas, is nevertheless very useful to test our understanding of CO₂ transport in the upper crust. Quantitative modeling of the radon signature, as presented in the companion paper [Girault and Perrier, 2014], sheds some light on the possible mechanisms present in such a hydrothermal system. Further models can now be developed and tested in the SBHS, models which must accommodate the observed spatial distribution and diversity of gas release in a heterogeneous site. Therefore, the SBHS also emerges as a natural analog of what can be expected in the case of leakage from a deep underground reservoir [e.g., Lewicki *et al.*, 2007; Koornneef *et al.*, 2012] in a context of interrelated fault and fracture networks.

Appendix A: Estimation of Total Discharge by Using a Small Number of Profiles and Measurement Points

When confronted with a potential gas zone, various problems occur in practice. The best strategy to assess whether a significant flux is present in the considered area might not be the optimal method to obtain a reasonable estimate of the total discharge [Cardellini *et al.*, 2003b; Rissmann *et al.*, 2012]. In some places, because of time constraints or local conditions such as cultivated areas, the number of possible measurements is limited, for example, to circa 40 points. Given these conditions, it is important to have some ideas of the optimal mapping method and the resulting accuracy that can be claimed on the discharge.

To test the estimation of the total CO₂ discharge in an unknown potential gas zone using a relatively small number of measurement points, we used a Monte Carlo method. In this calculation, a synthetic gas zone was

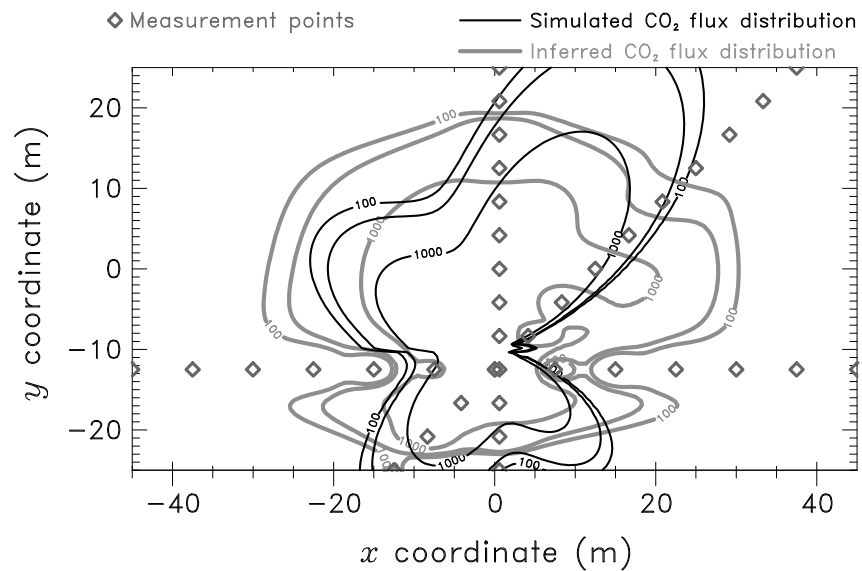


Figure A1. Monte Carlo simulation of the estimation of the total discharge using an adaptive strategy with 40 measurement points organized into two perpendicular profiles and one diagonal. The contours of the true discharge (2.22 t d^{-1}) are displayed in black while the inferred contours, drawn from interpolating the measured flux, are shown in gray. The obtained total discharge in this case is 2.28 t d^{-1} .

simulated in a 1200 m^2 space with a boundary where some background CO_2 flux was imposed. This synthetic zone was characterized by a total CO_2 degassing of the order of $1\text{--}3 \text{ t d}^{-1}$, typical of values obtained in the gas zones in the SBHS, and some shape of the spatial distribution was assumed. This shape was randomly modified in each set of cases of a given calculation. In this simulated zone, various strategies for the deployment of CO_2 flux measurements were performed, followed by methods for integration/aggregation. The results of each of these methods were compared with the synthetic total discharge, and their potential was assessed by dividing this estimation by the synthetic value. The hypothesis was to consider that the measurement technique is able to locally account for the real flux on the ground without any underestimation or overestimation, thus allowing for the known experimental uncertainties, but no systematic bias.

The first and simplest option was to measure CO_2 flux at points distributed randomly over the investigated surface. A second option was a simple mapping of flux over the whole area with a regular rectangular grid. These two options obviously have some difficulties when the number of possible measurements is small. In addition, it is unreasonable in practice to start some mapping strategy without knowing whether significant flux is present somewhere. Therefore, other approaches are implemented in real field conditions, mainly based on linear profiling. When some high flux is found on a profile, we then start mapping with new profiles crossing the first one, with different directions, and so on. Such adaptive approaches were tested using the Monte Carlo calculation. In a first strategy, two perpendicular profiles were used, the second profile passing through the highest CO_2 flux measured by the first profile, then supplemented with one diagonal profile. One example of such a strategy is shown in Figure A1, with 40 experimental points. Selected inferred interpolated contours are shown in gray and can be compared with the contours of the simulated source. The overall shape of the core zone with a flux higher than $1000 \text{ g m}^{-2} \text{ d}^{-1}$ inferred from the measurements is satisfactory and has an estimated area of 718 m^2 compared with a true area of 697 m^2 . In this particular case, the inferred total discharge is 2.7% above the simulated value. This method can be expanded to a method with the same number of points, but with two perpendicular diagonals, the second diagonal being centered at the barycenter of the fluxes from the first two profiles and the first diagonal.

These four methods are compared in Figure A2, which shows the mean difference between the inferred and the true discharge, as a function of the number of points. When the number of points is small, both the method with random points and that with a regular grid tend to underestimate the total discharge, but both methods converge to the true discharge as the number of points increases and are within a few percent of

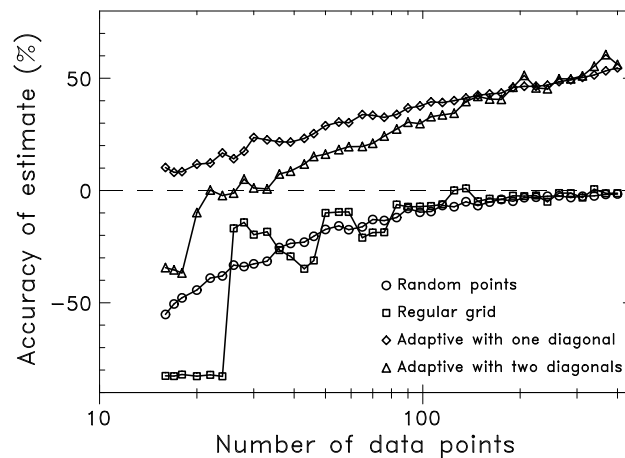


Figure A2. Accuracy of the inferred discharge, defined as the mean difference, over 200 simulations, between the inferred and the true discharge, as a function of the number of data points. Four methods are compared: randomly scattered points (circles), regular grid (squares), an adaptive method with two perpendicular profiles and one diagonal (diamonds), and a method with two diagonals (triangles).

the true discharge when the number of points is greater than circa 200. When the number of points is fewer than circa 20, the random distribution performs better than the regular grid, which can significantly underestimate the discharge. This is due to the fact that the regular grid with few points is too coarse given the size chosen for the source core. By contrast, the adaptive methods, which tend to overestimate the discharge, appear more accurate for small numbers of measurement points. In this case, with fewer than 40 measurement points, the adaptive method with two diagonals is best, while the method with one diagonal appears acceptable.

Such results have to be taken with caution. While they are reasonably stable when the interpolation method is changed, for example by varying the

order of the interpolation, they are not totally robust when the shape of the source is modified. In Figure A2, we have assumed a reasonably smooth shape with possible lobes, but with azimuthal variations of order smaller than 4 (Figure A1). When narrow lobes are allowed over a large fraction of the considered spatial scales, or if narrow rectangular slits are allowed, then the results displayed in Figure A2 can change, with underestimates lower than 50% for the random and the regular grids and overestimates larger than 80% in some cases for the adaptive techniques, which overly favor the highest fluxes.

In practice, the points with the highest fluxes can be difficult or impossible to measure, because of obstacles such as large boulders or unstable slopes, and some fraction of the gas release is therefore missing in the overall measured budget. It is therefore better, in any case, to use a method which tends to overestimate than a method which underestimates. In practice, one tends to complement linear profiles with additional points, or include additional constraints such as zero flux over the surface of a large boulder or a wall and to incorporate additional boundaries in the interpolation. At the end, the inferred contours need to be reasonably acceptable given the complications of the natural site. The Monte Carlo simulations in all cases nevertheless indicate that the method with adaptive profiles is satisfactory and that it is reasonable to quadratically add an additional uncertainty of 20% to the experimental punctual uncertainty (from flux measurements) to obtain the total uncertainty to account for possible systematic bias in the interpolation.

One important matter when calculating the total integrated discharge over a certain area is the role of boundaries. In the best cases, as in the case of GZ1, we obtain very similar discharge values and interpolated contours for CO_2 fluxes higher than $500 \text{ g m}^{-2} \text{ d}^{-1}$, either when imposing the background level at the boundary of the zone or when this condition is released (Text S3.3 in the supporting information). It is not always the case, and ultimately, the need of conditions at the boundaries can only rely on some knowledge of the site. As a final test of our calculation, we used the CO_2 flux data given by Parks *et al.* [2013], and we obtain CO_2 discharge values within 10% of the values given by these authors.

References

- Ader, T., *et al.* (2012), Convergence rate across the Nepal Himalaya and interseismic coupling on the Main Himalayan Thrust: Implications for seismic hazard, *J. Geophys. Res.*, *117*, B04403, doi:10.1029/2011JB009071.
- Ague, J. J. (2000), Release of CO_2 from carbonate rocks during regional metamorphism of lithologically heterogeneous crust, *Geology*, *28*(12), 1123–1126.
- Angell, R. F., T. Svejcar, J. Bates, N. Z. Saliendra, and D. A. Johnson (2001), Bowen ratio and closed chamber carbon dioxide flux measurements over sagebrush steppe vegetation, *Agric. For. Meteorol.*, *108*, 153–161.

Acknowledgments

The authors thank Som Sapkota and the Department of Mines and Geology (Kathmandu, Nepal) for continuous and enthusiastic support over the years. Buddha Lama, Dawa Tamang, Nabin Tamang, Gautam Tamang, Niraj Jairu, Khem Puri, and Hiralal Tamang are thanked for their assistance during the experiments. Patrick Richon is thanked for his initial help with the radon time series. André Revil is thanked for his inspiring encouragements and contributions during the early stage of this work. Caroline Guilmette is thanked for her valuable help in the measurement of carbon isotopic ratios in CRPG. Gauthier Hulot and Édouard Kaminski are thanked for their support to this program, which could be carried out, at its initial stage, thanks to a grant from the Fluids-Fault-Flux program of CNRS, followed by an interdisciplinary project from Université Paris Diderot (France). The original version of the manuscript was greatly improved, thanks to the careful work and numerous thoughtful suggestions of the Associate Editor, Cynthia Werner, and three anonymous reviewers. This is IPGP contribution number 3522.

- Annunziatellis, A., S. E. Beaubien, S. Bigi, G. Ciotoli, M. Coltella, and S. Lombardi (2008), Gas migration along fault systems and through the vadose zone in the Latera caldera (central Italy): Implications for CO₂ geological storage, *Int. J. Greenhouse Gas Control*, *2*, 353–372.
- Avouac, J.-P. (2003), Mountain building, erosion, and the seismic cycle in the Nepal Himalaya, *Adv. Geophys.*, *46*, 1–80.
- Avouac, J.-P., L. Bollinger, J. Lavé, R. Cattin, and M. Flouzat (2001), Le cycle sismique en Himalaya, *C. R. Acad. Sci.*, *333*, 513–529.
- Awasthi, K. D., B. K. Sitaula, B. R. Singh, and R. M. Bajracharya (2005), Fluxes of methane and carbon dioxide from soil under forest, grazing land, irrigated rice and rainfed field crops in a watershed of Nepal, *Biol. Fertil. Soils*, *41*, 163–172.
- Bateson, L., M. Vellico, S. E. Beaubien, J. M. Pearce, A. Annunziatellis, G. Ciotoli, F. Coren, S. Lombardi, and S. Marsh (2008), The application of remote-sensing techniques to monitor CO₂-storage sites for surface leakage: Method development and testing at Latera (Italy) where naturally produced CO₂ is leaking to the atmosphere, *Int. J. Greenhouse Gas Control*, *2*, 388–400.
- Baubron, J. C., P. Allard, and J. P. Toutain (1990), Diffuse volcanic emissions of carbon dioxide from Vulcano Island, Italy, *Nature*, *344*, 51–53.
- Becker, J. A. (2005), Quantification of Himalayan metamorphic CO₂ fluxes: Impact on global carbon budgets, PhD thesis, Univ. of Cambridge, Cambridge, U. K.
- Becker, J. A., M. J. Bickle, A. Galy, and T. J. B. Holland (2008), Himalayan metamorphic CO₂ fluxes: Quantitative constraints from hydrothermal springs, *Earth Planet. Sci. Lett.*, *265*, 616–629.
- Bellante, G. J., S. L. Powell, R. L. Lawrence, K. S. Repasky, and T. A. O. Dougher (2013), Aerial detection of a simulated CO₂ leak from a geologic sequestration site using hyperspectral imagery, *Int. J. Greenhouse Gas Control*, *13*, 124–137.
- Bergfeld, D., F. Goff, and C. J. Janik (2001), Elevated carbon dioxide flux at the Dixie Valley geothermal field, Nevada; relations between surface phenomena and the geothermal reservoir, *Chem. Geol.*, *177*, 43–66.
- Bergfeld, D., W. C. Evans, J. F. Howle, and C. D. Farrar (2006), Carbon dioxide emissions from vegetation-kill zones around the resurgent dome of Long Valley caldera, eastern California, U.S.A., *J. Volcanol. Geotherm. Res.*, *152*, 140–156.
- Bettinelli, P., J.-P. Avouac, M. Flouzat, F. Jouanne, L. Bollinger, P. Willis, and G. R. Chitrakar (2006), Plate motion of India and interseismic strain in the Nepal Himalaya from GPS and Doris measurements, *J. Geod.*, *80*, 567–589.
- Beysac, O., L. Bollinger, J.-P. Avouac, and B. Goffé (2004), Thermal metamorphism in the lesser Himalaya of Nepal determined from Raman spectroscopy of carbonaceous material, *Earth Planet. Sci. Lett.*, *225*, 233–241.
- Bollhöfer, A., J. Storm, P. Martin, and S. Tims (2006), Geographic variability in radon exhalation at a rehabilitated uranium mine in the Northern Territory, Australia, *Environ. Monit. Assess.*, *114*, 313–330.
- Bollinger, L., J.-P. Avouac, R. Cattin, and M. R. Pandey (2004), Stress buildup in the Himalaya, *J. Geophys. Res.*, *109*, B11405, doi:10.1029/2003JB002911.
- Bräuer, K., H. Kämpf, G. Strauch, and S. M. Weise (2003), Isotopic evidence (³He/⁴He, ¹³C_{CO₂}) of fluid-triggered intraplate seismicity, *J. Geophys. Res.*, *108*(B2), 2070, doi:10.1029/2002JB002077.
- Bräuer, K., H. Kämpf, U. Koch, S. Niedermann, and G. Strauch (2007), Seismically induced changes of the fluid signature detected by a multi-isotope approach (He, CO₂, CH₄, N₂) at the Wettinquelle, Bad Brambach (central Europe), *J. Geophys. Res.*, *112*, B04307, doi:10.1029/2006JB004404.
- Bräuer, K., H. Kämpf, S. Niedermann, G. Strauch, and J. Tesar (2008), Natural laboratory NW Bohemia: Comprehensive fluid studies between 1992 and 2005 used to trace geodynamic processes, *Geochem. Geophys. Geosyst.*, *9*, Q04018, doi:10.1029/2007GC001921.
- Bräuer, K., H. Kämpf, and G. Strauch (2009), Earthquake swarms in non-volcanic regions: What fluids have to say, *Geophys. Res. Lett.*, *36*, L17309, doi:10.1029/2009GL039615.
- Bräuer, K., H. Kämpf, U. Koch, and G. Strauch (2011), Monthly monitoring of gas and isotope compositions in the free gas phase at degassing locations close to the Nový Kostel focal zone in the western Eger Rift, Czech Republic, *Chem. Geol.*, *290*, 163–176.
- Bräuer, K., H. Kämpf, S. Niedermann, and G. Strauch (2013), Indications for the existence of different magmatic reservoirs beneath the Eifel area (Germany): A multi-isotope (C, N, He, Ne, Ar) approach, *Chem. Geol.*, *356*, 193–208.
- Breitner, D., H. Arvela, K.-H. Hellmuth, and T. Renvall (2010), Effect of moisture content on emanation at different grain size fractions – A pilot study on granitic esker sand sample, *J. Environ. Radioact.*, *101*, 1002–1006.
- Bréon, F.-M., and P. Ciais (2010), Spaceborne remote sensing of greenhouse gas concentrations, *C. R. Geosci.*, *342*, 412–424.
- Burton, M. R., G. M. Sawyer, and D. Granieri (2013), Deep carbon emissions from volcanoes, *Rev. Mineral. Geochem.*, *75*, 323–354.
- Byrdina, S., et al. (2009), Dipolar self-potential anomaly associated with carbon dioxide and radon flux at Syabru-Bensi hot springs in central Nepal, *J. Geophys. Res.*, *114*, B10101, doi:10.1029/2008JB006154.
- Carapezza, M. L., and L. Tarchini (2007), Accidental gas emission from shallow pressurized aquifers at Alban Hills volcano (Rome, Italy): Geochemical evidence of magmatic degassing?, *J. Volcanol. Geotherm. Res.*, *165*, 5–16.
- Carapezza, M. L., T. Ricci, M. Ranaldi, and L. Tarchini (2009), Active degassing structures of Stromboli and variations in diffuse CO₂ output related to the volcanic activity, *J. Volcanol. Geotherm. Res.*, *182*, 231–245.
- Carapezza, M. L., et al. (2011), Diffuse CO₂ soil degassing and CO₂ and H₂S concentrations in air and related hazards at Vulcano Island (Aeolian arc, Italy), *J. Volcanol. Geotherm. Res.*, *207*, 130–144.
- Carapezza, M. L., et al. (2012), Hazardous gas emissions from the flanks of the quiescent Colli Albani volcano (Rome, Italy), *Appl. Geochem.*, *27*, 1767–1782.
- Cardellini, C., G. Chiodini, F. Frondini, D. Granieri, J. Lewicki, and L. Peruzzi (2003a), Accumulation chamber measurements of methane fluxes: Application to volcanic-geothermal areas and landfills, *Appl. Geochem.*, *18*, 45–54.
- Cardellini, C., G. Chiodini, and F. Frondini (2003b), Application of stochastic simulation to CO₂ flux from soil: Mapping and quantification of gas release, *J. Geophys. Res.*, *108*(B9), 2425, doi:10.1029/2002JB002165.
- Chacko, T., T. K. Mayeda, R. N. Clayton, and J. R. Goldsmith (1991), Oxygen and carbon isotope fractionations between CO₂ and calcite, *Geochim. Cosmochim. Acta*, *55*(10), 2867–2882.
- Chiodini, G., R. Cioni, M. Guidi, B. Raco, and L. Marini (1998), Soil CO₂ flux measurements in volcanic and geothermal areas, *Appl. Geochem.*, *13*(5), 543–552.
- Chiodini, G., F. Frondini, D. M. Kerrick, J. Rogie, F. Parello, L. Peruzzi, and A. R. Zanzari (1999), Quantification of deep CO₂ fluxes from Central Italy. Examples of carbon balance for regional aquifers and of soil diffuse degassing, *Chem. Geol.*, *159*, 205–222.
- Chiodini, G., F. Frondini, C. Cardellini, D. Granieri, L. Marini, and G. Ventura (2001), CO₂ degassing and energy release at Solfatara volcano, Campi Flegrei, Italy, *J. Geophys. Res.*, *106*(B8), 16,213–16,221.
- Chiodini, G., R. Avino, T. Brombach, S. Caliro, C. Cardellini, S. De Vita, F. Frondini, D. Granieri, E. Marotta, and G. Ventura (2004), Fumarolic and diffuse soil degassing west of Mount Epomeo, Ischia, Italy, *J. Volcanol. Geotherm. Res.*, *133*, 291–309.
- Chiodini, G., D. Granieri, R. Avino, S. Caliro, and A. Costa (2005), Carbon dioxide diffuse degassing and estimation of heat release from volcanic and hydrothermal systems, *J. Geophys. Res.*, *110*, B08204, doi:10.1029/2004JB003542.

- Chiodini, G., A. Baldini, F. Barberi, M. L. Carapezza, C. Cardellini, F. Frondini, D. Granieri, and M. Ranaldi (2007), Carbon dioxide degassing at LATERA caldera (Italy): Evidence of geothermal reservoir and evaluation of its potential energy, *J. Geophys. Res.*, *112*, B12204, doi:10.1029/2006JB004896.
- Chiodini, G., D. Granieri, R. Avino, S. Caliro, A. Costa, C. Minopoli, and G. Vilardo (2010), Non-volcanic CO₂ Earth degassing: Case of Mefite d'Ansanto (southern Apennines), Italy, *Geophys. Res. Lett.*, *37*, L11303, doi:10.1029/2010GL042858.
- Ciotoli, G., S. Lombardi, and A. Annunziatellis (2007), Geostatistical analysis of soil gas data in a high seismic intermontane basin: Fucino Plain, central Italy, *J. Geophys. Res.*, *112*, B05407, doi:10.1029/2005JB004044.
- Collé, R. (1995), Critically evaluated half-life for ²²²Rn radioactive decay and associated uncertainties, *Radioact. Radiochem.*, *6*(1), 30–40.
- Crockett, R. G. M., and G. K. Gillmore (2010), Spectral-decomposition techniques for the identification of radon anomalies temporally associated with earthquakes occurring in the UK in 2002 and 2008, *Nat. Hazards Earth Syst. Sci.*, *10*, 1079–1084.
- Crockett, R. G. M., G. K. Gillmore, P. S. Phillips, A. R. Denman, and C. J. Groves-Kirkby (2006), Radon anomalies preceding earthquakes which occurred in the UK, in summer and autumn 2002, *Sci. Total Environ.*, *364*, 138–148.
- Cullen, T. L. (1946), On the exhalation of radon from the Earth, *Terr. Magn. Atmos. Electr.*, *51*, 37–44.
- D'Alessandro, W., L. Brusca, K. Kyriakopoulos, S. Rotolo, G. Michas, M. Minio, and G. Papadakis (2006), Diffuse and focused carbon dioxide and methane emissions from the Sousaki geothermal system, Greece, *Geophys. Res. Lett.*, *33*, L05307, doi:10.1029/2006GL025777.
- D'Alessandro, W., L. Brusca, K. Kyriakopoulos, G. Michas, and G. Papadakis (2008), Methana, the westernmost active volcanic system of the south Aegean arc (Greece): Insight from fluids geochemistry, *J. Volcanol. Geotherm. Res.*, *178*, 818–828.
- Das, N. K., D. Ghose, and B. Sinha (1998), Radon emission from hydrothermal springs at Tantloi, *Radiat. Phys. Chem.*, *51*(4–6), 611–612.
- Derry, L. A., M. J. Evans, R. Darling, and C. France-Lanord (2009), Hydrothermal heat flow near the Main Central Thrust, central Nepal Himalaya, *Earth Planet. Sci. Lett.*, *286*, 101–109.
- Di Napoli, R., et al. (2011), The structure of a hydrothermal system from an integrated geochemical, geophysical, and geological approach: The Ischia Island case study, *Geochem. Geophys. Geosyst.*, *12*, Q07017, doi:10.1029/2010GC003476.
- Duchemin, B., N. Coursol, and M. M. Bé (1994), The re-evaluation of decay data for the U-238 chain, *Nucl. Instrum. Methods*, *A339*, 146–150.
- Etiopie, G. (1999), Subsoil CO₂ and CH₄ and their advective transfer from faulted grassland to the atmosphere, *J. Geophys. Res.*, *104*(D14), 16,889–16,894.
- Etiopie, G., and S. Lombardi (1995), Evidence for radon transport by carrier gas through faulted clays in Italy, *J. Radioanal. Nucl. Chem.*, *193*(2), 291–300.
- Etiopie, G., P. Beneduce, M. Calcara, P. Favali, F. Frugoni, M. Schiattarella, and G. Smriglio (1999), Structural pattern and CO₂-CH₄ degassing of Ustica Island, Southern Tyrrhenian basin, *J. Volcanol. Geotherm. Res.*, *88*, 291–304.
- Evans, M. J., L. A. Derry, and C. France-Lanord (2004), Geothermal fluxes of alkalinity in the Narayani river system of central Nepal, *Geochem. Geophys. Geosyst.*, *5*, Q08011, doi:10.1029/2004GC000719.
- Evans, M. J., L. A. Derry, and C. France-Lanord (2008), Degassing of metamorphic carbon dioxide from the Nepal Himalaya, *Geochem. Geophys. Geosyst.*, *9*, Q04021, doi:10.1029/2007GC001796.
- Evans, W. C., D. Bergfeld, R. G. McGimsey, and A. G. Hunt (2009), Diffuse gas emissions at the Ukinrek Maars, Alaska: Implications for magmatic degassing and volcanic monitoring, *Appl. Geochem.*, *24*, 527–535.
- Farrar, C. D., M. L. Sorey, W. C. Evans, J. F. Howle, B. D. Kerr, B. M. Kennedy, C.-Y. King, and J. R. Southon (1995), Forest-killing diffuse CO₂ emission at Mammoth Mountain as a sign of magmatic unrest, *Nature*, *376*, 675–678.
- Favara, R., S. Giammanco, S. Inguaggiato, and G. Pecoraino (2001), Preliminary estimate of CO₂ output from Pantelleria Island volcano (Sicily, Italy): Evidence of active mantle degassing, *Appl. Geochem.*, *16*, 883–894.
- Federico, C., M. Camarda, S. De Gregorio, and S. Gurrieri (2011), Long-term record of CO₂ degassing along Mt. Etna's flanks and its relationship with magma dynamics and eastern flank instability, *Geochem. Geophys. Geosyst.*, *12*, Q10002, doi:10.1029/2011GC003601.
- Ferry, C., A. Beneito, P. Richon, and M.-C. Robé (2001), An automatic device for measuring the effect of meteorological factors on radon-222 flux from soils in the long term, *Radiat. Prot. Dosim.*, *93*(3), 271–274.
- Finizola, A., et al. (2010), Adventive hydrothermal circulation on Stromboli volcano (Aeolian Islands, Italy) revealed by geophysical approaches: Implications for general fluid flow models on volcanoes, *J. Volcanol. Geotherm. Res.*, *196*, 111–119.
- Fridriksson, T., B. R. Kristjánsson, H. Ármannsson, E. Margrétardóttir, S. Ólafsdóttir, and G. Chiodini (2006), CO₂ emissions and heat flow through soil, fumaroles, and steam heated mud pools at the Reykjanes geothermal area, SW Iceland, *Appl. Geochem.*, *21*, 1551–1569.
- Gaillardet, J., and A. Galy (2008), Himalaya - Carbon Sink or Source?, *Science*, *320*, 1727–1728.
- Geller, R. J. (2011), Shake-up time for Japanese seismology, *Nature*, *472*, 407–409.
- Gerlach, T. M. (2011), Volcanic versus anthropogenic carbon dioxide, *EOS Trans. AGU*, *92*(24), 201–208.
- Gerlach, T. M., M. P. Doukas, K. A. McGee, and R. Kessler (2001), Soil efflux and total emission rates of magmatic CO₂ at the Horseshoe Lake tree kill, Mammoth Mountain, California, *Chem. Geol.*, *177*, 101–116.
- Ghosh, D., A. Deb, and R. Sengupta (2009), Anomalous radon emission as precursor of earthquake, *J. Appl. Geophys.*, *69*, 67–81.
- Giammanco, S., S. Gurrieri, and M. Valenza (1995), Soil CO₂ degassing on Mt Etna (Sicily) during the period 1989–1993: Discrimination between climatic and volcanic influences, *Bull. Volcanol.*, *57*, 52–60.
- Giammanco, S., F. Parello, B. Gambardella, R. Schifano, S. Pizzullo, and G. Galante (2007), Focused and diffuse effluxes of CO₂ from mud volcanoes and mofettes south of Mt. Etna (Italy), *J. Volcanol. Geotherm. Res.*, *165*, 46–63.
- Giammanco, S., M. Palano, A. Scaltrito, L. Scarfi, and F. Sortino (2008), Possible role of fluid overpressure in the generation of earthquake swarms in active tectonic areas: The case of the Peloritani Mts. (Sicily, Italy), *J. Volcanol. Geotherm. Res.*, *178*, 795–806.
- Giammanco, S., F. Bellotti, G. Groppelli, and A. Pinton (2010), Statistical analysis reveals spatial and temporal anomalies of soil CO₂ efflux on Mount Etna volcano (Italy), *J. Volcanol. Geotherm. Res.*, *194*, 1–14.
- Girault, F. (2011), Etude des flux de dioxyde de carbone et de radon dans l'Himalaya du Népal (in French), PhD thesis, Univ. Paris Diderot (Paris VII), Paris, France.
- Girault, F., and F. Perrier (2012), Measuring effective radium concentration with large numbers of samples. Part I – experimental method and uncertainties, *J. Environ. Radioact.*, *113*, 177–188.
- Girault, F., and F. Perrier (2014), The Syabru-Bensi hydrothermal system in central Nepal: 2. Modeling and significance of the radon signature, companion paper, *J. Geophys. Res. Solid Earth*, doi:10.1002/2013JB010302, in press.
- Girault, F., B. P. Koirala, F. Perrier, P. Richon, and S. Rajaura (2009), Persistence of radon-222 flux during monsoon at a geothermal zone in Nepal, *J. Environ. Radioact.*, *100*, 955–964.
- Girault, F., A. P. Gajurel, F. Perrier, B. N. Upreti, and P. Richon (2011a), Radon emanation of heterogeneous basin deposits in Kathmandu Valley, Nepal, *J. Asian Earth Sci.*, *40*, 595–610.
- Girault, F., C. Poitou, F. Perrier, B. P. Koirala, and M. Bhattarai (2011b), Soil characterization using patterns of magnetic susceptibility versus effective radium concentration, *Nat. Hazards Earth Syst. Sci.*, *11*(8), 2285–2293.

- Girault, F., F. Perrier, A. P. Gajurel, M. Bhattarai, B. P. Koirala, L. Bollinger, M. Fort, and C. France-Lanord (2012), Effective radium concentration across the Main Central Thrust in the Nepal Himalayas, *Geochim. Cosmochim. Acta*, *98*, 203–227.
- Goscombe, B., D. Gray, and M. Hand (2006), Crustal architecture of the Himalayan metamorphic front in eastern Nepal, *Gondwana Res.*, *10*, 232–255.
- Granieri, D., R. Avino, and G. Chiodini (2010), Carbon dioxide diffuse emission from the soil: Ten years of observations at Vesuvio and Campi Flegrei (Pozzuoli), and linkages with volcanic activity, *Bull. Volcanol.*, *72*, 103–118.
- Greeman, D. J., and A. W. Rose (1996), Factors controlling the emanation of radon and thoron in soils of the eastern U.S.A., *Chem. Geol.*, *129*, 1–14.
- Guillot, S. (1999), An overview of the metamorphic evolution in Central Nepal, *J. Asian Earth Sci.*, *17*, 713–725.
- Guillot, S., G. Mahéo, J. de Sigoyer, K. H. Hattori, and A. Pêcher (2008), Tethyan and Indian subduction viewed from the Himalayan high- to ultrahigh-pressure metamorphic rocks, *Tectonophysics*, *451*, 225–241.
- Hernández, P. A., N. M. Pérez, J. M. Salazar, S. Nakai, K. Notsu, and H. Wakita (1998), Diffuse emission of carbon dioxide, methane, and helium-3 from Teide volcano, Tenerife, Canary Islands, *Geophys. Res. Lett.*, *25*(17), 3311–3314.
- Hernández, P. A., J. M. Salazar, Y. Shimoike, T. Mori, K. Notsu, and N. Pérez (2001a), Diffuse emission of CO₂ from Miyakejima volcano, Japan, *Chem. Geol.*, *177*, 175–185.
- Hernández, P. A., K. Notsu, J. M. Salazar, T. Mori, G. Natale, H. Okada, G. Virgili, Y. Shimoike, M. Sato, and N. M. Pérez (2001b), Carbon dioxide degassing by advective flow from Usu volcano, Japan, *Science*, *292*, 83–86.
- Hernández, P. A., K. Notsu, M. Tsurumi, T. Mori, M. Ohno, Y. Shimoike, J. Salazar, and N. M. Pérez (2003), Carbon dioxide emissions from soils at Hakkoda, north Japan, *J. Geophys. Res.*, *108*(B4), 2210, doi:10.1029/2002JB001847.
- Hernández, P. A., K. Notsu, H. Okada, T. Mori, M. Sato, F. Barahona, and N. M. Pérez (2006), Diffuse emission of CO₂ from Showa-Shinzan, Hokkaido, Japan: A sign of volcanic dome degassing, *Pure Appl. Geophys.*, *163*, 869–881.
- Hernández, P. A., et al. (2012a), Analysis of long- and short-term temporal variations of the diffuse CO₂ emission from Timanfaya volcano, Lanzarote, Canary Islands, *Appl. Geochem.*, *27*, 2486–2499.
- Hernández, P. A., et al. (2012b), Diffuse volcanic degassing and thermal energy release from Hengill volcanic system, Iceland, *Bull. Volcanol.*, *74*, 2435–2448.
- Hoke, L., S. Lamb, D. R. Hilton, and R. J. Poreda (2000), Southern limit of mantle-derived geothermal helium emissions in Tibet: Implications for lithospheric structure, *Earth Planet. Sci. Lett.*, *180*, 297–308.
- Ielsch, G., D. Thiéblemont, V. Labeled, P. Richon, G. Tymen, C. Ferry, M. C. Robé, J. C. Baubron, and F. Béchenec (2001), Radon (²²²Rn) level variations on a regional scale: Influence of the basement trace element (U, Th) geochemistry on radon exhalation rates, *J. Environ. Radioact.*, *53*, 75–90.
- Ingersoll, J. G. (1983), A survey of radionuclide contents and radon emanation rates in building materials used in the U.S., *Health Phys.*, *45*(2), 363–368.
- Inguaggiato, S., A. Mazot, I. S. Diliberto, C. Inguaggiato, P. Madonia, D. Rouwet, and F. Vita (2012), Total CO₂ output from Vulcano Island (Aeolian Islands, Italy), *Geochem. Geophys. Geosyst.*, *13*, Q02012, doi:10.1029/2011GC003920.
- Ishimori, Y., and Y. Maruo (2005), Radon exhalation rate monitoring in/around the closed uranium mine sites in Japan, *Int. Congr. Ser.*, *1276*, 291–292.
- Italiano, F., M. Martelli, G. Martinelli, and P. M. Nuccio (2000), Geochemical evidence of melt intrusions along lithospheric faults of the Southern Apennines, Italy: Geodynamic and seismogenic implications, *J. Geophys. Res.*, *105*(B6), 13,569–13,578.
- Jha, S., A. H. Khan, and U. C. Mishra (2000), A study of the ²²²Rn flux from soil in the U mineralised belt at Jaduguda, *J. Environ. Radioact.*, *49*, 157–169.
- Jha, S., A. H. Khan, and U. C. Mishra (2001), A study of the technologically modified sources of ²²²Rn and its environmental impact in an Indian U mineralised belt, *J. Environ. Radioact.*, *53*, 183–197.
- Kämpf, H., K. Bräuer, J. Schumann, K. Hahne, and G. Strauch (2013), CO₂ discharge in an active, non-volcanic continental rift area (Czech Republic): Characterisation ($\delta^{13}\text{C}$, $^3\text{He}/^4\text{He}$) and quantification of diffuse and vent CO₂ emissions, *Chem. Geol.*, *339*, 71–83.
- King, C.-Y., W. Zhang, and Z. Zhang (2006), Earthquake-induced groundwater and gas changes, *Pure Appl. Geophys.*, *163*, 633–645.
- Klemperer, S. L., B. M. Kennedy, S. R. Sastry, Y. Makovsky, T. Harinarayana, and M. L. Leech (2013), Mantle fluids in the Karakoram fault: Helium isotope evidence, *Earth Planet. Sci. Lett.*, *366*, 59–70.
- Kohn, M. J. (2008), P-T-t data from central Nepal support critical taper and repudiate large-scale channel flow of the Greater Himalayan Sequence, *Geol. Soc. Am. Bull.*, *120*(3/4), 259–273.
- Kohn, M. J., S. K. Paul, and S. L. Corrie (2010), The lower Lesser Himalayan sequence: A Paleoproterozoic arc on the northern margin of the Indian plate, *Geol. Soc. Am. Bull.*, *122*(3/4), 323–335.
- Koornneef, J., A. Ramírez, W. Turkenburg, and A. Faaij (2012), The environmental impact and risk assessment of CO₂ capture, transport and storage – An evaluation of the knowledge base, *Prog. Energy Combust.*, *38*(1), 62–86.
- Kotarba, M. (1986), Hydrogeological investigations in Seti Khola and Trisuli thermal springs areas (Nepal Himalayas), *Geologia*, *12*, 37–51.
- Lan, T. F., T. F. Yang, H.-F. Lee, Y.-G. Chen, C.-H. Chen, S.-R. Song, and S. Tsao (2007), Compositions and flux of soil gas in Liu-Huang-Ku hydrothermal area, northern Taiwan, *J. Volcanol. Geotherm. Res.*, *165*, 32–45.
- Lavrova, T., and O. Voitsekhovaly (2013), Radioecological assessment and remediation planning at the former uranium milling facilities at the Pridnieprovsky Chemical Plant in Ukraine, *J. Environ. Radioact.*, *115*, 118–123.
- Lawrence, C. E., R. A. Akber, A. Bollhöfer, and P. Martin (2009), Radon-222 exhalation from open ground on and around a uranium mine in the wet-dry tropics, *J. Environ. Radioact.*, *100*, 1–8.
- Legaz, A., J. Vandemeulebrouck, A. Revil, A. Kemna, A. W. Hurst, R. Reeves, and R. Papsin (2009), A case study of resistivity and self-potential signatures of hydrothermal instabilities, Inferno Crater Lake, Waimangu, New Zealand, *Geophys. Res. Lett.*, *36*, L12306, doi:10.1029/2009GL037573.
- Lemonnier, C., G. Marquis, F. Perrier, J.-P. Avouac, G. Chitrakar, B. Kafle, S. Sapkota, U. Gautam, D. Tiwari, and M. Bano (1999), Electrical structure of the Himalaya of Central Nepal: High conductivity around the mid-crustal ramp along the MHT, *Geophys. Res. Lett.*, *26*(21), 3261–3264.
- Lewicki, J. L., and S. L. Brantley (2000), CO₂ degassing along the San Andreas fault, Parkfield, California, *Geophys. Res. Lett.*, *27*(1), 5–8.
- Lewicki, J. L., W. C. Evans, G. E. Hilley, M. L. Sorey, J. D. Rogie, and S. L. Brantley (2003a), Shallow soil CO₂ flow along the San Andreas and Calaveras Faults, California, *J. Geophys. Res.*, *108*(B4), 2187, doi:10.1029/2002JB002141.
- Lewicki, J. L., C. Connor, K. St-Amant, J. Stix, and W. Spinner (2003b), Self-potential, soil CO₂ flux, and temperature on Masaya volcano, Nicaragua, *Geophys. Res. Lett.*, *30*(15), 1817, doi:10.1029/2003GL017731.

- Lewicki, J. L., J. Birkholzer, and C.-F. Tsang (2007), Natural and industrial analogues for leakage of CO₂ from storage reservoirs: Identification of features, events, and processes and lessons learned, *Environ. Geol.*, *52*, 457–467.
- Lewicki, J. L., M. L. Fischer, and G. E. Hilley (2008), Six-week time series of eddy covariance CO₂ flux at Mammoth Mountain, California: Performance evaluation and role of meteorological forcing, *J. Volcanol. Geotherm. Res.*, *171*, 178–190.
- Lewicki, J. L., G. E. Hilley, L. Dobeck, and B. D. V. Marino (2012), Eddy covariance imaging of diffuse volcanic CO₂ emissions at Mammoth Mountain, CA, U.S.A., *Bull. Volcanol.*, *74*, 135–141.
- Lewicki, J. L., G. E. Hilley, L. Dobeck, T. L. McLing, B. M. Kennedy, M. Bill, and B. D. V. Marino (2013), Geologic CO₂ input into groundwater and the atmosphere, Soda Springs, ID, U.S.A., *Chem. Geol.*, *339*, 61–70.
- López-Coto, I., J. L. Mas, J. P. Bolívar, and R. García-Tenorio (2009), A short-time method to measure the radon potential of porous materials, *Appl. Radiat. Isot.*, *67*, 133–138.
- Lozano, J. C., F. Vera Tomé, V. Gómez Escobar, and P. Blanco Rodríguez (2000), Radiological characterization of a uranium mine with no mining activity, *Appl. Radiat. Isot.*, *53*, 337–343.
- Lucas, H. F. (1957), Improved Low-Level Alpha-Scintillation Counter for Radon, *Rev. Sci. Instrum.*, *28*(9), 680–683.
- Macfarlane, A. M., K. V. Hodges, and D. Lux (1992), A structural analysis of the Main Central Thrust zone, Langtang National Park, central Nepal Himalaya, *Geol. Soc. Am. Bull.*, *104*, 1389–1402.
- Manga, M., I. Beresnev, E. E. Brodsky, J. E. Elkhoury, D. Elsworth, S. E. Ingebritsen, D. C. Mays, and C.-Y. Wang (2012), Changes in permeability caused by transient stresses: Field observations, experiments, and mechanisms, *Rev. Geophys.*, *50*, RG2004, doi:10.1029/2011RG000382.
- Manning, C. E., and S. E. Ingebritsen (1999), Permeability of the continental crust: Implications of geothermal data and metamorphic systems, *Rev. Geophys.*, *37*(1), 127–150.
- Marty, B., C. France-Lanord, A. Gajurel, R. Mural, F. Vuatz, and P. Le Fort (1996), CO₂ and Helium in mineral springs of Nepal and Mustang: A study of volatile release processes during the Himalayan tectonics, Abstracts of the 11th Himalaya-Karakoram-Tibet Conference, Northern Arizona Univ., Flagstaff AZ, U.S.A., 97–98.
- Mazot, A., D. Rouwet, Y. Taran, S. Inguaggiato, and N. Varley (2011), CO₂ and He degassing at El Chichón volcano, Chiapas, Mexico: Gas flux, origin and relationship with local and regional tectonics, *Bull. Volcanol.*, *73*, 423–441.
- Mazot, A., E. R. Smid, L. Schwendenmann, H. Delgado-Granados, and J. Lindsay (2013), Soil CO₂ flux baseline in an urban monogenetic volcanic field: The Auckland Volcanic Field, New Zealand, *Bull. Volcanol.*, *75*, 757.
- Mazzini, A., H. Svensen, G. Etiope, N. Onderdonk, and D. Banks (2011), Fluid origin, gas fluxes and plumbing system in the sediment-hosted Salton Sea Geothermal System (California, U.S.A.), *J. Volcanol. Geotherm. Res.*, *205*, 67–83.
- Megumi, K., and T. Mamuro (1974), Emanation and exhalation of radon and thoron gases from soil particles, *J. Geophys. Res.*, *79*(23), 3357–3360.
- Meslin, P. Y., J.-C. Sabroux, S. Bassot, and E. Chassefière (2011), Experimental study of radon production and transport in an analogue for the Martian regolith, *Geochim. Cosmochim. Acta*, *75*, 2256–2270.
- Mook, W. G., J. C. Bommerson, and W. H. Staverman (1974), Carbon isotope fractionation between dissolved bicarbonate and gaseous carbon dioxide, *Earth Planet. Sci. Lett.*, *22*, 169–176.
- Mörner, N.-A., and G. Etiope (2002), Carbon degassing from the lithosphere, *Global Planet. Change*, *33*, 185–203.
- Mudd, G. M. (2008), Radon releases from Australian uranium mining and milling projects: Assessing the UNSCEAR approach, *J. Environ. Radioact.*, *99*, 288–315.
- Nazaroff, W. W. (1992), Radon transport from soil to air, *Rev. Geophys.*, *30*(2), 137–160.
- Newell, D. L., M. J. Jessup, J. M. Cottle, D. R. Hilton, Z. D. Sharp, and T. P. Fischer (2008), Aqueous and isotope geochemistry of mineral springs along the southern margin of the Tibetan plateau: Implications for fluid sources and regional degassing of CO₂, *Geochem. Geophys. Geosyst.*, *9*, Q08014, doi:10.1029/2008GC002021.
- Notsu, K., K. Sugiyama, M. Hosoe, A. Uemura, Y. Shimoike, F. Tsunomori, H. Sumino, J. Amamoto, T. Mori, and P. A. Hernández (2005), Diffuse CO₂ efflux from Iwojima volcano, Izu-Ogasawara arc, Japan, *J. Volcanol. Geotherm. Res.*, *139*, 147–161.
- Padrón, E., P. A. Hernández, T. Toulkeridis, N. M. Pérez, R. Marrero, G. Melián, G. Virgili, and K. Notsu (2008), Diffuse CO₂ emission rate from Pulumahua and the lake-filled Cuicocha calderas, Ecuador, *J. Volcanol. Geotherm. Res.*, *176*, 163–169.
- Padrón, E., P. A. Hernández, N. M. Pérez, T. Toulkeridis, G. Melián, J. Barrancos, G. Virgili, H. Sumino, and K. Notsu (2012), Fumarole/plume and diffuse CO₂ emission from Sierra Negra caldera, Galapagos archipelago, *Bull. Volcanol.*, *74*, 1509–1519.
- Pandey, M. R., R. P. Tandukar, J.-P. Avouac, J. Lavfi, and J. P. Massot (1995), Interseismic strain accumulation on the Himalayan crustal ramp (Nepal), *Geophys. Res. Lett.*, *22*(7), 751–754.
- Pandey, M. R., R. P. Tandukar, J.-P. Avouac, J. Vergne, and T. Héritier (1999), Seismotectonics of the Nepal Himalaya from a local seismic network, *J. Asian Earth Sci.*, *17*, 703–712.
- Parks, M. M., S. Caliro, G. Chiodini, D. M. Pyle, T. A. Mather, K. Berlo, M. Edmonds, J. Biggs, P. Nomikou, and C. Raptakis (2013), Distinguishing contributions to diffuse CO₂ emissions in volcanic areas from magmatic degassing and thermal decarbonation using soil gas ²²²Rn-δ¹³C systematics: Application to Santorini volcano, Greece, *Earth Planet. Sci. Lett.*, *377*–378, 180–190.
- Parrish, R. R., and K. V. Hodges (1996), Isotopic constraints on the age and provenance of the Lesser and Greater Himalayan sequences, Nepalese Himalaya, *Geol. Soc. Am. Bull.*, *108*(7), 904–911.
- Pearson, J. E., and G. E. Jones (1966), Soil concentrations of "emanating radium-226" and the emanation of radon-222 from soils and plants, *Tellus*, *18*(2), 655–662.
- Pearson, O. N., and P. G. DeCelles (2005), Structural geology and regional tectonic significance of the Ramgarh thrust, Himalayan fold-thrust belt of Nepal, *Tectonics*, *24*, TC4008, doi:10.1029/2003TC001617.
- Pecoraino, G., L. Brusca, W. D'Alessandro, S. Giammanco, S. Inguaggiato, and M. Longo (2005), Total CO₂ output from Ischia Island volcano (Italy), *Geochem. J.*, *39*, 451–458.
- Pérez, N. M., et al. (2011), Global CO₂ emission from volcanic lakes, *Geology*, *39*(3), 235–238.
- Perrier, F., M. Trique, B. Lorne, J.-P. Avouac, S. Hautot, and P. Tarits (1998), Electric potential variations associated with yearly lake level variations, *Geophys. Res. Lett.*, *25*(11), 1955–1958.
- Perrier, F., M. Trique, J. Aupiais, U. Gautam, and P. Shrestha (1999), Electric potential variations associated with periodic spring discharge in western Nepal, *C. R. Acad. Sci.*, *328*, 73–79.
- Perrier, F., et al. (2009), A direct evidence for high carbon dioxide and radon-222 discharge in Central Nepal, *Earth Planet. Sci. Lett.*, *278*, 198–207.
- Reth, S., M. Göckede, and E. Falge (2005), CO₂ efflux from agricultural soils in Eastern Germany – comparison of a closed chamber system with eddy covariance measurements, *Theor. Appl. Climatol.*, *80*, 105–120.
- Revil, A., M. Karaoulis, T. Johnson, and A. Kemna (2012), Review: Some low-frequency electrical methods for subsurface characterization and monitoring in hydrogeology, *Hydrogeol. J.*, *20*, 617–658.

- Richon, P., F. Perrier, J.-C. Sabroux, M. Trique, C. Ferry, V. Voisin, and E. Pili (2005), Spatial and time variations of radon-222 concentration in the atmosphere of a dead-end horizontal tunnel, *J. Environ. Radioact.*, *78*(2), 179–198.
- Richon, P., Y. Klinger, P. Tapponnier, C.-X. Li, J. Van Der Woerd, and F. Perrier (2010), Measuring radon flux across active faults: Relevance of excavating and possibility of satellite discharges, *Radiat. Meas.*, *45*, 211–218.
- Richon, P., F. Perrier, B. P. Koirala, F. Girault, M. Bhattarai, and S. N. Sapkota (2011), Temporal signatures of advective versus diffusive radon transport at a geothermal zone in Central Nepal, *J. Environ. Radioact.*, *102*, 88–102.
- Rinaldi, A. P., J. Vandemeulebrouck, M. Todesco, and F. Viveiros (2012), Effects of atmospheric conditions on surface diffuse degassing, *J. Geophys. Res.*, *117*, B11201, doi:10.1029/2012JB009490.
- Rissmann, C., B. Christenson, C. Werner, M. Leybourne, J. Cole, and D. Gravley (2012), Surface heat flow and CO₂ emissions within the Ohaaki hydrothermal field, Taupo Volcanic Zone, New Zealand, *Appl. Geochem.*, *27*, 223–239.
- Rizzo, A., et al. (2009), Geochemical evaluation of observed changes in volcanic activity during the 2007 eruption at Stromboli (Italy), *J. Volcanol. Geotherm. Res.*, *182*, 246–254.
- Rodrigo-Naharro, J., B. Nisi, O. Vaselli, M. Lelli, R. Saldaña, C. Clemente-Jul, and L. Pérez del Villar (2013), Diffuse soil CO₂ flux to assess the reliability of CO₂ storage in the Mazarrón-Gañuelas Tertiary Basin (Spain), *Fuel*, *114*, 162–171.
- Rogie, J. D., D. M. Kerrick, G. Chiodini, and F. Frondini (2000), Flux measurements of nonvolcanic emission from some vents in central Italy, *J. Geophys. Res.*, *105*(B4), 8435–8445.
- Rojstaczer, S. A., S. E. Ingebritsen, and D. O. Hayba (2008), Permeability of continental crust influenced by internal and external forcing, *Geofluids*, *8*, 128–139.
- Sahoo, B. K., Y. S. Mayya, B. K. Sapra, J. J. Gaware, K. S. Banerjee, and H. S. Kushwaha (2010), Radon exhalation studies in an Indian uranium tailings pile, *Radiat. Meas.*, *45*, 237–241.
- Sakoda, A., Y. Ishimori, and K. Yamaoka (2011), A comprehensive review of radon emanation measurements for mineral, rock, soil, mill tailing and fly ash, *Appl. Radiat. Isot.*, *69*, 1422–1435.
- Salazar, J. M. L., P. A. Hernández, N. M. Pérez, G. Melián, J. Álvarez, F. Segura, and K. Notsu (2001), Diffuse emission of carbon dioxide from Cerro Negro volcano, Nicaragua, Central America, *Geophys. Res. Lett.*, *28*(22), 4275–4278.
- Sapkota, S. N., L. Bollinger, Y. Klinger, P. Tapponnier, Y. Gaudemer, and D. Tiwari (2013), Primary surface ruptures of the great Himalayan earthquakes in 1934 and 1255, *Nat. Geosci.*, *6*, 71–76.
- Schery, S. D., S. Whittlestone, K. P. Hart, and S. E. Hill (1989), The flux of radon and thoron from Australian soils, *J. Geophys. Res.*, *94*(D6), 8567–8576.
- Searle, M. P., R. D. Law, L. Godin, K. P. Larson, M. J. Streule, J. M. Cottle, and M. J. Jessup (2008), Defining the Himalayan Main Central Thrust in Nepal, *J. Geol. Soc. London*, *165*, 523–534.
- Shimoike, Y., K. Kazahaya, and H. Shinohara (2002), Soil gas emission of volcanic CO₂ at Satsuma-Iwojima volcano, Japan, *Earth Planets Space*, *54*, 239–247.
- Siebert, L., and T. Simkin (2002), *Volcanoes of the world: An illustrated catalogue of Holocene volcanoes and their eruptions*, Smithsonian Institution, Global Volcanism Program Digital Information Series, GVP-3. [Available at <http://www.volcano.si.edu/world/>]
- Singh, H., J. Singh, S. Singh, and B. S. Bajwa (2008), Radon exhalation rate and uranium estimation study of some soil and rock samples from Tusham ring complex, India using SSNTD technique, *Radiat. Meas.*, *43*, S459–S462.
- Somlai, J., Z. Gorjánház, A. Várhegyi, and T. Kovács (2006), Radon concentration in houses over a closed Hungarian uranium mine, *Sci. Total Environ.*, *367*, 653–665.
- Stoulos, S., M. Manolopoulou, and C. Papastefanou (2003), Assessment of natural radiation exposure and radon exhalation from building materials in Greece, *J. Environ. Radioact.*, *69*, 225–240.
- Stoulos, S., M. Manolopoulou, and C. Papastefanou (2004), Measurement of radon emanation factor from granular samples: Effects of additives in cement, *Appl. Radiat. Isot.*, *60*, 49–54.
- Szegvary, T., M. C. Leuenberger, and F. Conen (2007), Predicting terrestrial ²²²Rn flux using gamma dose rate as a proxy, *Atmos. Chem. Phys.*, *7*, 2789–2795.
- Takagi, H., K. Arita, T. Sawaguchi, K. Kobayashi, and D. Awaji (2003), Kinematic history of the Main Central Thrust zone in the Langtang area, Nepal, *Tectonophysics*, *366*, 151–163.
- Tan, K., Z. Liu, L. Xia, J. Lv, and H. Hu (2012), The influence of fractal size distribution of covers on radon exhalation from uranium mill tailings, *Radiat. Meas.*, *47*, 163–167.
- Tanner, A. B. (1964), Radon migration in the ground: A review, in *The Natural Radiation Environment*, edited by J. A. S. Adams and W. M. Lowder, pp. 161–190, Univ. of Chicago Press, Chicago.
- Tassi, F., B. Nisi, C. Cardellini, F. Capecchiacci, M. Donnini, O. Vaselli, R. Avino, and G. Chiodini (2013), Diffuse soil emission of hydrothermal gases (CO₂, CH₄, and C₆H₆) at Solfatara crater (Campi Flegrei, southern Italy), *Appl. Geochem.*, *35*, 142–153.
- Toutain, J.-P., and J.-C. Baubron (1999), Gas geochemistry and seismotectonics: A review, *Tectonophysics*, *304*, 1–27.
- Toutain, J.-P., F. Sortino, J.-C. Baubron, P. Richon, Surono, S. Sumarti, and A. Nonell (2009), Structure and CO₂ budget of Merapi volcano during inter-eruptive periods, *Bull. Volcanol.*, *71*, 815–826.
- Tuccimei, P., and M. Soligo (2008), Correcting for CO₂ interference in soil radon flux measurements, *Radiat. Meas.*, *43*, 102–105.
- Upreti, B. N. (1999), An overview of the stratigraphy and tectonics of the Nepal Himalaya, *J. Asian Earth Sci.*, *17*, 577–606.
- Virk, H. S., and B. Singh (1994), Radon recording of Uttarkashi earthquake, *Geophys. Res. Lett.*, *21*(8), 737–740.
- Viveiros, F., T. Ferreira, C. Silva, and J. L. Gaspar (2009), Meteorological factors controlling soil gases and indoor CO₂ concentration: A permanent risk in degassing area, *Sci. Total Environ.*, *407*, 1362–1372.
- Viveiros, F., C. Cardellini, T. Ferreira, S. Caliro, G. Chiodini, and C. Silva (2010), Soil CO₂ emissions at Furnas volcano, São Miguel Island, Azores archipelago: Volcano monitoring perspectives, geomorphologic studies, and land use planning application, *J. Geophys. Res.*, *115*, B12208, doi:10.1029/2010JB007555.
- Vodnik, D., U. Videmsek, M. Pintar, I. Macek, and H. Pfanzer (2009), The characteristics of soil CO₂ fluxes at a site with natural CO₂ enrichment, *Geoderma*, *150*, 32–37.
- Voltattorni, N., A. Sciarra, G. Caramanna, D. Cinti, L. Pizzino, and F. Quattrocchi (2009), Gas geochemistry of natural analogues for the studies of geological CO₂ sequestration, *Appl. Geochem.*, *24*, 1339–1346.
- Walia, V., H. S. Virk, and B. S. Bajwa (2006), Radon precursory signals for some earthquakes of magnitude > 5 occurred in N-W Himalaya: An overview, *Pure Appl. Geophys.*, *163*, 711–721.
- Wardell, L. J., P. R. Kyle, N. Dunbar, and B. Christenson (2001), White Island volcano, New Zealand: Carbon dioxide and sulfur dioxide emission rates and melt inclusion studies, *Chem. Geol.*, *177*, 187–200.
- Weise, S. M., K. Bräuer, H. Kämpf, G. Strauch, and U. Koch (2001), Transport of mantle volatiles through the crust traced by seismically released fluids: A natural experiment in the earthquake swarm area Vogtland/NW Bohemia, Central Europe, *Tectonophysics*, *336*, 137–150.

- Welles, J. M., T. H. Demetriades-Shah, and D. K. McDermitt (2001), Considerations for measuring ground CO₂ effluxes with chambers, *Chem. Geol.*, *177*, 3–13.
- Werner, C., and C. Cardellini (2006), Comparison of carbon dioxide emissions with fluid upflow, chemistry, and geologic structures at the Rotorua geothermal system, New Zealand, *Geothermics*, *35*, 221–238.
- Werner, C., S. L. Brantley, and K. Boomer (2000), CO₂ emissions related to the Yellowstone volcanic system. 2. Statistical sampling, total degassing, and transport mechanisms, *J. Geophys. Res.*, *105*(B5), 10,831–10,846.
- Werner, C., G. Chiodini, D. Voigt, S. Caliro, R. Avino, M. Russo, T. Brombach, J. Wyngaard, and S. Brantley (2003), Monitoring volcanic hazard using eddy covariance at Solfatara volcano, Naples, Italy, *Earth Planet. Sci. Lett.*, *210*, 561–577.
- Werner, C., S. Hurwitz, W. C. Evans, J. B. Lowenstern, D. Bergfeld, H. Heasler, C. Jaworowski, and A. Hunt (2008), Volatile emissions and gas geochemistry of Hot Spring Basin, Yellowstone National Park, U.S.A., *J. Volcanol. Geotherm. Res.*, *178*, 751–762.
- Williams-Jones, G., J. Stix, M. Heiligmann, A. Charland, B. Sherwood Lollar, N. Arner, G. Garzón, J. Barquero, and E. Fernandez (2000), A model of diffuse degassing at three subduction-related volcanoes, *Bull. Volcanol.*, *62*, 130–142.
- Yang, T. F., H.-Y. Wen, C.-C. Fu, H.-F. Lee, T. F. Lan, A.-T. Chen, W.-L. Hong, S.-J. Lin, and V. Wallia (2011), Soil radon flux and concentrations in hydrothermal area of the Tatun Volcano Group, Northern Taiwan, *Geochem. J.*, *45*, 483–490.
- Yokoyama, T., S. Nakai, and H. Wakita (1999), Helium and carbon isotopic compositions of hot spring gases in the Tibetan Plateau, *J. Volcanol. Geotherm. Res.*, *88*, 99–107.
- Žunić, Z. S., et al. (2006), High natural radiation exposure in radon spa areas: A detailed field investigation in Niška Banja (Balkan region), *J. Environ. Radioact.*, *89*, 249–260.